

**PCCP**

**Bulk properties of aqueous graphene oxide and reduced graphene oxide with surfactants and polymers: adsorption and stability**

Journal:	<i>Physical Chemistry Chemical Physics</i>
Manuscript ID	CP-ART-04-2018-002738.R1
Article Type:	Paper
Date Submitted by the Author:	01-Jun-2018
Complete List of Authors:	McCoy, Thomas; Monash University, School of Chemistry de Campo, Liliana; ANSTO, ACNS Sokolova, Anna; ANSTO, ACNS Grillo, Isabelle; Institut Max-Von-Laue-Paul-Langevin, Pas, Ekaterina; Monash University, School of Chemistry Tabor, Rico; Monash University, School of Chemistry

SCHOLARONE™  
Manuscripts



Cite this: DOI: 10.1039/xxxxxxxxxx

# Bulk properties of aqueous graphene oxide and reduced graphene oxide with surfactants and polymers: adsorption and stability<sup>†</sup>

Thomas M. McCoy,<sup>a</sup> Liliana de Campo,<sup>b</sup> Anna V. Sokolova,<sup>b</sup> Isabelle Grillo,<sup>c</sup> Ekaterina I. Izgorodina<sup>a</sup> and Rico F. Tabor,<sup>\*a</sup>

Received Date

Accepted Date

DOI: 10.1039/xxxxxxxxxx

www.rsc.org/journalname

A diverse range of molecular surfactants and polymers have been incorporated into aqueous graphene oxide (GO) and reduced graphene oxide (rGO) dispersions in order to understand the complex relationship between surface chemistry, surface forces and interfacial thermodynamics of these materials with typical amphiphiles. Surfactant additives were systematically varied in terms of their charge and hydrophobicity to reveal important structure–function relationships affecting adsorption and interaction with GO and rGO surfaces. Small-angle (and ultra small-angle) neutron scattering was employed to examine and monitor the interactions and self-assembly in each system. Charge was found to be the overriding factor driving adsorption, as cationic surfactants very readily adsorbed to both GO and rGO, whereas anionic surfactants gave little to no evidence of adsorption despite possessing hydrophobic tail-groups. Molecules of neutral charge such as nonionic and zwitterionic surfactants as well as neutral polymers also showed strong affinities for GO and rGO, indicating that dispersion and dipole (induction polarisation) interactions also play a significant role in adsorption with these materials. Modelling the neutron data revealed in many cases a  $q^{-2}$  slope in the low  $q$  and ultra low  $q$  regions, indicating that scattering was occurring from large, flat surfaces (lamellae or bilayers), suggesting an effective flattening of the sheets in dispersion. The results presented thus help to form a roadmap for the behaviour of GO and rGO with surfactants and polymers, relevant to adsorption, stabilisation, formulation and coating in aqueous environments as adsorbent and functional materials.

## 1 Introduction

Graphene oxide (GO) and reduced graphene oxide (rGO) have continued to gain considerable research momentum in recent years owing to their great potential in a wide variety of fields and applications. Unlike pristine graphene, which is composed of pure carbon,<sup>1,2</sup> GO and rGO have the useful benefit of being processable in aqueous solution due to their chemical functionalisation with oxygenated groups.<sup>3–5</sup> This feature, combined with their exceptional surface area to mass ratio, make GO and rGO sheets ideal substrates in applications where adsorption is a central process.<sup>6–8</sup> Such areas

include emulsification,<sup>9–11</sup> foaming,<sup>12–15</sup> coating,<sup>16–18</sup> self-assembly<sup>19–21</sup> and adsorption/decontamination;<sup>22</sup> the findings put forward in this study are most significantly applicable to the latter two phenomena.

GO is highly compatible with water, and as such can form concentrated dispersions and even hydrogels.<sup>23,24</sup> The aggressive oxidation of graphite using the improved Hummers' method (used in this work),<sup>25</sup> results in a large proportion of oxygen being introduced to the graphene sheets (up to 40% by mass), in the form of epoxy, hydroxy and carboxy groups.<sup>3</sup> GO sheets are thus exceptionally hydrophilic and exhibit large negative surface potentials in water, readily resulting in their dispersion through favourable solvation and electrostatic repulsions.<sup>26,27</sup> However when reduced with hydrazine,<sup>5</sup> aromaticity on the basal plains of the sheets is largely restored, and the oxygen content controllably decreases down to approximately 20% by mass, resulting in a material intermediate between graphene and GO in terms of electrical, mechanical and adsorption properties. Therefore, rGO sheets are inherently more hydrophobic, and only form stable suspensions up to 0.5 mg/mL, despite retaining

<sup>a</sup> School of Chemistry, Monash University, Clayton 3800, VIC, Australia. Fax: +61 3 9905 4597; Tel: +61 3 9905 4558; E-mail: rico.tabor@monash.edu

<sup>b</sup> Australian Centre for Neutron Scattering, ANSTO, Lucas Heights 2234, NSW, Australia.

<sup>c</sup> Institut Laue-Langevin, F-38042 Grenoble, France.

<sup>†</sup> Electronic Supplementary Information (ESI) available: [contains further information on models, fitting parameters and sample characterisation]. See DOI: 10.1039/b000000x/

significant negative surface charge.<sup>5</sup> The effective hydrophilic–lipophilic balance of these materials is thus a significant factor influencing their dispersion and adsorption properties,<sup>28</sup> and realistically limits the use of rGO in aqueous applications.<sup>29</sup> However, deposition of rGO from water has been found to be effective in technological processing, from anti-corrosion layers<sup>30,31</sup> to supercapacitors<sup>32,33</sup> and batteries<sup>34–37</sup>.

In spite of substantial research into the applications and chemistry of GO and rGO as adsorbent materials,<sup>6–8,22</sup> a clear understanding of their physical behaviour and interactions with small molecules in solution has not been obtained. For instance, contention exists surrounding the interfacial properties and surface activity of GO and rGO, specifically on whether their behaviour is more akin to that of molecular surfactants or amphiphilic particles, with most works suggesting the former.<sup>9,20,28,38</sup> Theoretical chemistry computations, including molecular dynamics, density functional theory and *ab initio*, have been performed on model systems of GO and rGO to assist in understanding their electronic structure, surface chemistry, and wettability.<sup>27,39–42</sup> However, the relationship between these important aspects of GO and rGO chemistry, and the way that these materials interact with myriad organic and inorganic compounds, remains poorly characterised. Further investigation of aqueous GO and rGO dispersions with molecular additives and the key criteria for adsorption are thus required before the commercialisation and application of these materials in areas such as industrial wastewater treatment and oil recovery becomes viable.

In this work, we directly examine the response of aqueous suspensions of GO and rGO to a variety of carefully selected molecular surfactants and polymers. Using a combination of small and ultra-small-angle neutron scattering (SANS and USANS), we have monitored *in situ* the interactions and assembly of these compounds with the carbon nanomaterials at nano and microscopic length scales. The surfactant additives vary in terms of their head-group chemistry, in order to understand the effects of charge sign and hydrophilicity, and tail-groups to control hydrophobicity and saturation (to explore  $\pi$ – $\pi$ -stacking effects with GO/rGO basal plane). Through this systematic variation, the effects of electrostatic, polarisation and hydrophobic (dispersion forces) interactions on the adsorption and co-assembly of the surfactants with both GO and rGO can be compared. Thus, we are able to gain insight into the fundamental physicochemical phenomena underpinning the behaviour and basis for GO and rGO as aqueous adsorbents, so that predictions can be made, and more effective deployment of these materials in industrial applications can be achieved.

## 2 Experimental

### Materials

Graphene oxide was synthesised from graphite flakes (Sigma, +100 mesh) by the improved method of Marcano *et al.*<sup>25</sup>. Minor modifications to the procedure included an incremental addition of the potassium permanganate prior to heating the mixture, and purification by 3 cycles of centrifugation (4000 rpm), redispersing

the particles in ultrapure water only, followed by dialysis for 1 week (cellulose dialysis tubing, 12,800 Da molecular weight cut-off, Sigma). The product was kept and characterised as an aqueous suspension. Reduction of the GO followed Li *et al.*,<sup>5</sup> with the product also purified by dialysis in ultrapure water. Characterisation of these materials has been performed previously and can be found in the Electronic Supplementary Information of McCoy *et al.*<sup>43</sup>

Cetyltrimethylammonium bromide (CTAB,  $\geq 99\%$ ) was from ChemSupply and dodecyltrimethylammonium bromide (DTAB,  $\geq 98\%$ ) and tetradecyltrimethylammonium bromide (TTAB,  $\geq 98\%$ ) were from Sigma. Hexaethylene glycol monododecyl ether (C<sub>12</sub>E<sub>6</sub>), pentaethylene glycol monododecyl ether (C<sub>12</sub>E<sub>5</sub>) and tetraethylene glycol monododecyl ether (C<sub>12</sub>E<sub>4</sub>), all  $\geq 98\%$ , were from Sigma. Triton X-100 (TX-100,  $\geq 98\%$ ) and sodium dodecyl sulphate (SDS, 90%) were from ChemSupply. Sodium bis(2-ethylhexyl) sulfosuccinate (AOT, 96%) was from ACROS Organics. Each of these surfactants were used as received with the exception of SDS which was recrystallised once from hot ethanol. Erucyl amidopropyl betaine (EAPB) and oleyl amidopropyl betaine (OAPB) were synthesised and purified as described previously.<sup>44–46</sup> Polyethylene glycol or oxide (PEG, M<sub>v</sub> = 400,000 g/mol) and Pluronic F-127 were from Sigma.

### Methods

Small-angle neutron scattering (SANS) measurements were undertaken on two instruments: D11 (Institut Laue-Langevin, Grenoble, France) and Bilby<sup>47</sup> (Australian Centre for Neutron Scattering, Lucas Heights, Australia). Samples were prepared using D<sub>2</sub>O as the solvent and measured in 2 mm path-length Hellma cells at room temperature (25°C). The radially isotropic raw counts from the detectors were reduced to radially averaged absolute intensity profiles as a function of the scattering vector,  $q$ , defined as

$$q = \frac{4\pi}{\lambda} \sin \frac{\theta}{2}$$

where  $\theta$  is the scattering angle and  $\lambda$  is the wavelength of the incident neutrons. Bilby is a time-of-flight SANS instrument, hence the instrument utilises a range of wavelengths, in this case  $\lambda = 2\text{--}20 \text{ \AA}$ , to obtain spatiotemporal information about the sample. The main detector was positioned 6 m from the samples while the four curtain detectors were 3 m (left and right detectors) and 4 m (top and bottom detector), giving a  $q$ -range of approximately  $0.002\text{--}0.6 \text{ \AA}^{-1}$ . In the process of reduction, the raw data were normalised against a transmission measurement and the background was corrected using a blocked beam measurement. Scaling for absolute intensities was achieved by accounting for the sample thickness (2 mm) and using an empty beam measurement. Scattering from an empty cell (for pure surfactant samples) or D<sub>2</sub>O sample (for samples containing GO or rGO) was subtracted prior to modelling data. The D11 SANS instrument was used to obtain the scattering of the pure GO dispersions (ILL data citation: doi-10.5291/ILL-DATA.9-10-1309). For D11, two configurations were used with  $\lambda = 10 \text{ \AA}$ , with a wavelength spread defined by  $\Delta\lambda/\lambda = 9\%$ , and sample–detector distances of 1.2 and 8 m, with a detector offset to provide

a  $q$ -range of 0.003–0.387  $\text{\AA}^{-1}$ .

Ultra-small-angle neutron scattering (USANS) measurements were made using the Kookaburra beamline<sup>48,49</sup> at the Australian Centre for Neutron Scattering, ANSTO. The instrument features a Bense-Hart setup in which two parallel arrays of quintuple-reflection channel-cut silicon crystals serve to monochromate and analyse the beam.<sup>50</sup> A wavelength of 4.74  $\text{\AA}$  was used in these measurements and depending on run time, could obtain data over a  $q$ -range of 0.00005–0.005  $\text{\AA}^{-1}$  (0.1–10  $\mu\text{m}$  length scales). Desmearing of the data was then performed using a specially developed Igor Pro package<sup>51</sup> before stitching with the relevant SANS data.

Modelling of scattering data was performed using the software 'SasView' (<http://www.sasview.org>). In some instances when combining SANS and USANS, a scale factor was applied to the USANS data in order to align with the corresponding SANS data, made necessary by fluctuations in incident beam intensity and desmearing effects. For all data presented throughout, symbols represent the raw experimental scattering data, and solid lines are model fits generated as described in the text. Vertical error bars are present in all data sets, but in most instances are too small to see. All fitting parameters from the models are presented in the Electronic Supplementary Information, including further details on the models themselves and modelling procedures.

Atomic force microscopy (AFM) was performed using a JPK NanoWizard 3. Imaging was carried out in AC mode with Bruker NCHV model cantilevers with spring constants of *ca.* 42 N/m and nominal resonant frequencies of *ca.* 340 kHz. Samples were prepared by spin-coating (60 s, 2000 rpm) approximately 3–5  $\mu\text{L}$  of 0.1 mg/mL GO or rGO onto freshly cleaved mica disks (ProSciTech). For samples with polymer, the 0.1 mg/mL GO or rGO dispersions also included 0.1 or 0.5 mg/mL of PEG or Pluronic F127. Images were refined using the JPK Data Processing software and lateral dimensions for GO and rGO sheets were measured using Gwyddion (<http://gwyddion.net>).<sup>52</sup>

### 3 Results and discussion

#### Graphene oxide and reduced graphene oxide

Small-angle scattering is not a commonly exploited technique for examining and characterising two-dimensional carbon nanomaterials. Small-angle x-ray scattering (SAXS) has been used to characterise graphite oxide (3D stack) prepared by various known methods,<sup>53</sup> however the low electron densities of the elements make analysing dilute solutions of graphene oxide (GO, single layer) difficult by SAXS, and the very low proportion of hydrogen (<2%)<sup>3</sup> also offers poor contrast using SANS with solvent contrast variation. In all SANS data sets presented in this work, 0.1 mg/mL of GO or rGO is used, and the observed scattering from the carbon nanomaterials themselves in each case is minimal (Fig. 1a). Atomic force microscopy (AFM) imaging (in air) revealed monolayer nanosheets ( $\approx 1$  nm thickness) for both GO and rGO (Fig. 1b–e), with average lateral sizes of 0.338 and 0.407  $\mu\text{m}$  respectively (Fig. 1f,g). These materials are therefore within the length regime accessible to SANS and USANS (1 nm–10  $\mu\text{m}$ ). The wrinkling of rGO (Fig. 1c) is likely a result of the

drying process for imaging. The increased hydrophobicity of rGO sheets causes them to fold and clump together through strong  $\pi$ - $\pi$ -stacking interactions. Large clusters of rGO could also be observed in some regions of the AFM samples (see ESI).

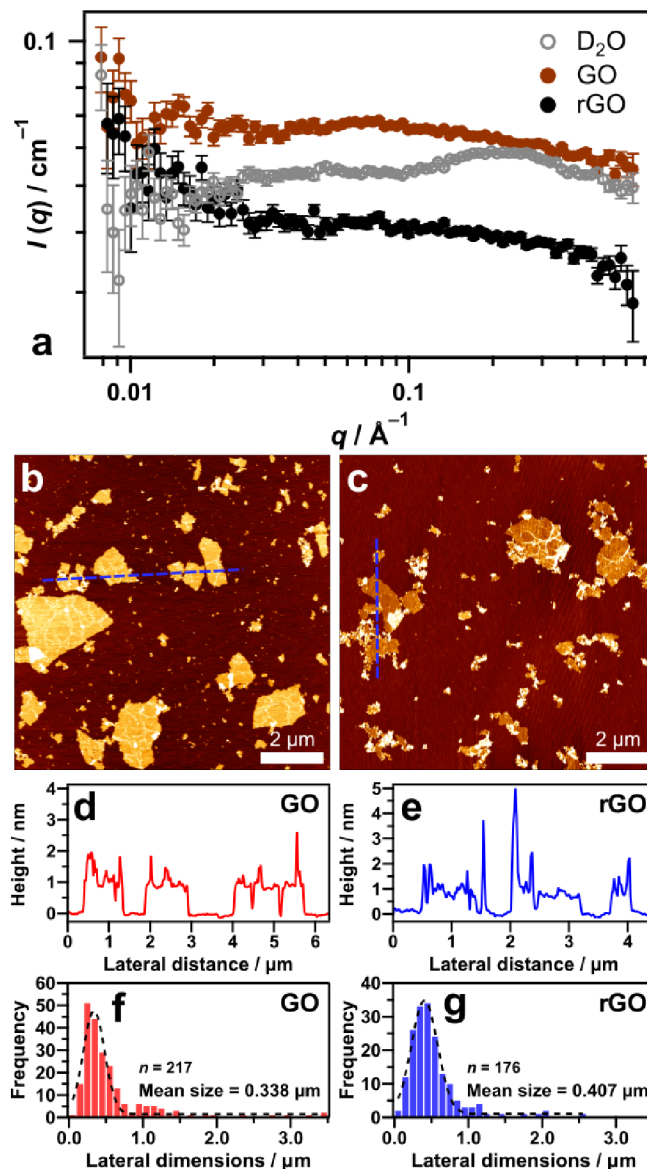


**Fig. 1** (a) SANS data of 0.1 mg/mL GO and rGO following  $\text{D}_2\text{O}$  background subtractions. Note that the suspensions were diluted with  $\text{D}_2\text{O}$  from concentrated suspensions in  $\text{H}_2\text{O}$ . Hence, a  $\text{D}_2\text{O}$  background was subtracted from these data sets rather than an empty cell background, as the baseline scatter from GO and rGO samples were marginally higher due to containing approximately 3%  $\text{H}_2\text{O}$ . Data for  $\text{D}_2\text{O}$  has had scattering from an empty cell subtracted. Data for GO is offset by multiplication for clarity ( $\times 2$ ). (b & c) AFM height images of GO and rGO dried on mica respectively. (d & e) Height profiles of GO and rGO respectively where each cross section corresponds to the dashed blue line on the image above. (f & g) Histograms of the lateral dimensions of GO and rGO sheets respectively. Data is binned to 100 nm and  $n$  is the total number of observations.

In order to model the scattering for pure aqueous GO dispersions, a mass fractal model was employed (Fig. 2).<sup>54</sup> The mass fractal model approximates the scattering of spatially

inhomogeneous objects according to a power law, allowing determination of the fractal dimensionality  $D_m$  of the material. This provides a statistical index of how aggregated or structurally complex the material/assembly is over the measured length scale (higher fractal dimension corresponds to higher complexity).<sup>54,55</sup> As carbon and oxygen have similar scattering length densities ( $6.65$  and  $5.80 \times 10^{-6} \text{ \AA}^{-2}$  respectively) to that of  $\text{D}_2\text{O}$  ( $6.34 \times 10^{-6} \text{ \AA}^{-2}$ ), the scattering contrast for GO originates from the proportion of hydrogen which is only small in these materials (<2% by mass).<sup>3</sup> Therefore, the hydrogen atoms serve as the scattering 'building blocks' or particle radius for the mass fractal structure, hence, this parameter is treated as negligible (see ESI for fitting parameters). The modelling of the GO SANS data reveals mass fractal dimensions of approximately 2.8 (see ESI, Table S1), with the slopes at low  $q$  being around 3.2 (Fig. 2), indicating that the sheets have a semi-aggregated, crumpled morphology when dispersed on their own in aqueous solution.<sup>56-58</sup>

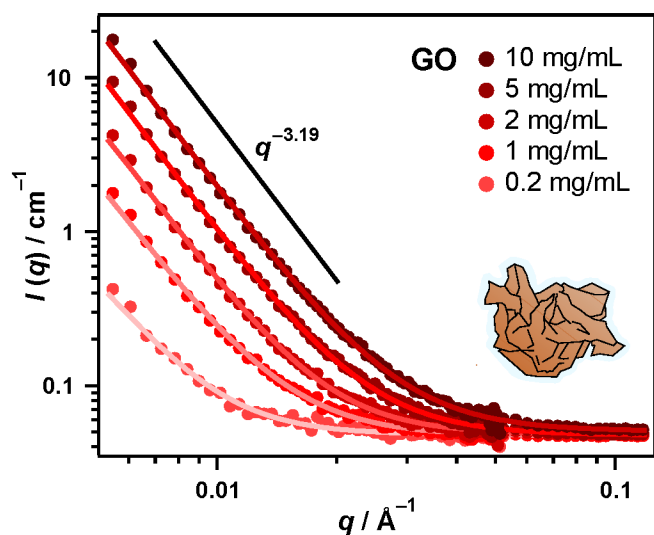


**Fig. 2** SANS data of GO in water at increasing concentrations. Symbols are raw data points and solid lines are the mass fractal model fits. Inset is the proposed 'crumpled' structure for GO sheet morphology in solution, as determined by the slope at low  $q$ .

As scattering from the GO sheets themselves becomes significantly greater at higher concentrations (Fig. 2), GO and rGO concentrations of  $0.1 \text{ mg/mL}$  were used in all subsequent measurements. In this case, scattering contrast for neutrons is thus expected to arise from the surfactant molecules added to the aqueous GO and rGO dispersions. The use of surfactants therefore not only gives insight into molecular interactions with these carbon nanomaterials for understanding adsorption, but also allows selective 'highlighting' of the sheets. Thus, their precise morphologies can be determined without convolution of the data from multiple scattering sources.

### Interactions with cationic surfactants

Cationic magnetic surfactants have been shown to destabilise GO and form noncovalent magneto-responsive composites that can be used as recoverable materials in wastewater purification.<sup>59</sup>

Likewise, a cationic photo-switchable surfactant can be used for reversible, light-controllable separation and redispersion of rGO.<sup>43</sup> Cationic surfactants have also even been exploited to enhance the surface activity of GO sheets and facilitate their enrichment at interfaces,<sup>60</sup> resulting in improved capacity for emulsion stabilisation,<sup>61</sup> and recovery by froth flotation.<sup>62,63</sup> In all cases, the positively charged head-group ensures a strong electrostatic attraction with the negatively charged GO and rGO sheets, resulting in significant levels of adsorption. Therefore, we first explored the effects of cationic surfactants in aqueous dispersions of GO and rGO. For this, a classic and well characterised series of surfactants with trimethylammonium head-groups was chosen: cetyltrimethylammonium bromide (hexadecyltrimethylammonium bromide, CTAB), tetradecyltrimethylammonium bromide (TTAB) and dodecyltrimethylammonium bromide (DTAB). The lengths of the alkyl chains vary from 16, 14 and 12 carbons respectively (Fig. 4d), so that the hydrophobic contribution to the molecular interactions could also be assessed.

As cationic surfactants bear an opposing charge to GO and rGO sheets in solution, there is a propensity for the carbon materials to flocculate within a specific range of carbon nanomaterial:surfactant ratios due to reduction in magnitude of the interparticle repulsive forces.<sup>43,61</sup> SANS measurements *in situ* may be ineffective or misleading when used on unstable or inhomogeneous systems. Therefore it was necessary to map the stability of the colloidal suspension across a broad range of concentration ratios to uncover where the system was stable/unstable, and thus determine which sample compositions were suitable for analysis by SANS.

Stability phase diagrams for DTAB, TTAB and CTAB with GO were determined (Fig. 3) in which a total of 20 different sample compositions were assessed for each surfactant (see ESI, Fig. S4-S6). Samples were deemed stable if no aggregation could be observed, metastable if partial aggregation and sedimentation over 24 hours could be observed, and unstable if the GO was completely flocculated (Fig. 3a). Depending on the surfactant, the initial onset of GO aggregation with increasing surfactant loading was found to occur at lower surfactant concentrations with increasing tail-group length (Fig. 3b-d, CTAB < TTAB < DTAB). This effect is likely due to the higher surface activity associated with the longer tail-groups causing adsorption onto the GO surfaces and subsequent destabilisation to occur more readily. In turn, colloidal restabilisation of the GO was also found to occur at lower surfactant concentrations for the longer chain molecules (Fig. 3b-d). Stability of the GO at increased surfactant loadings can be attributed to charge reversal of the sheets from adsorbed cationic surfactant, such that the materials are now stabilised through positive charge repulsions.<sup>61</sup> As CTAB is more surface active than TTAB and DTAB, larger quantities adsorb to the GO sheets, hence the restabilisation effect is observed at lower surfactant concentrations with increasing tail-group length. The same can be said for TTAB when compared to DTAB. Interestingly, this effect also appears to coincide with the critical micelle concentrations (CMC) for each surfactant (see ESI, Fig. S3),<sup>64,65</sup> reaffirming that the behaviour is a hydrophobic

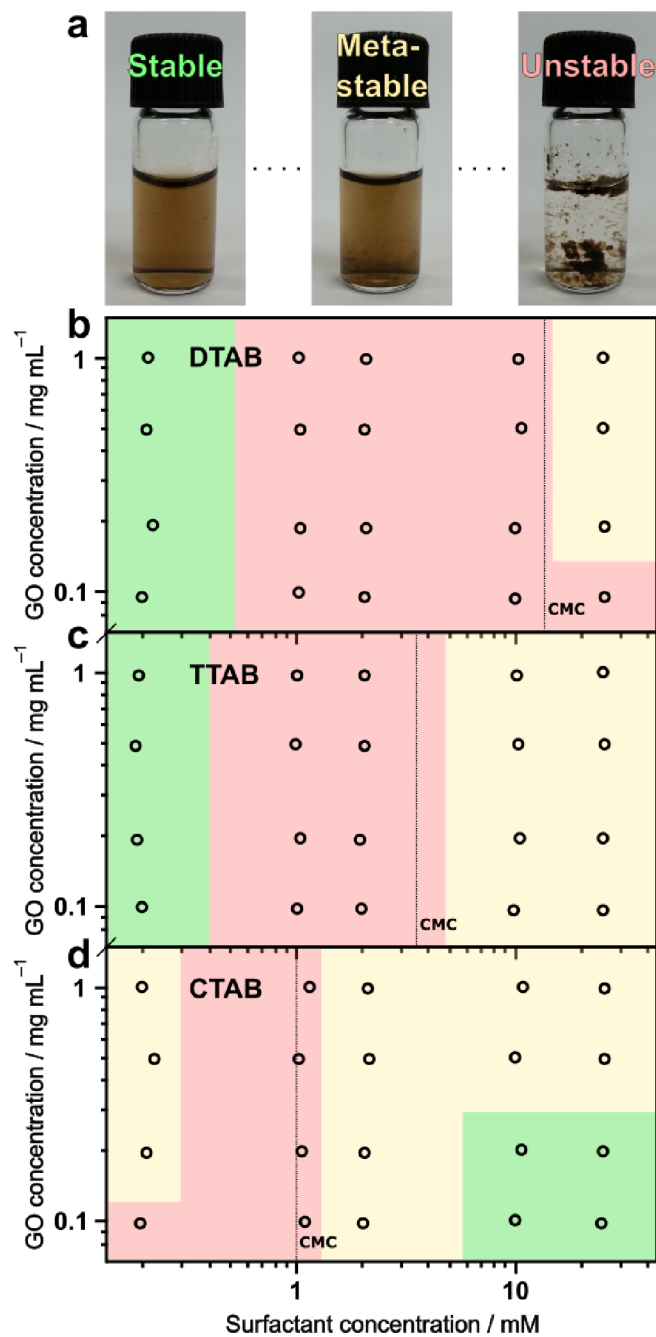


**Fig. 3** (a) Samples of TTAB and GO with phase behaviour specified as stable, metastable and unstable. (b-d) Stability phase diagrams of aqueous graphene oxide dispersions with DTAB (b), TTAB (c) and CTAB (d). The green regions signify stable systems, while the yellow and red regions represent metastable (partially flocculated) and unstable (flocculated) systems. The circles signify specific individual samples (see ESI, Figs. S4-6) from which the borders between phases were estimated. The vertical dashed lines mark the approximate critical micelle concentrations (CMC) for each surfactant as determined from surface tension measurements (see ESI, Fig. S3).

phenomenon. The phase behaviour indicates that hydrophobic interactions (dispersion forces) also play a significant role in adsorption and interactions within these systems, and that charge is not the only factor governing the bulk and interfacial properties of GO in the presence of adsorbing molecules.

With these effects in mind, high DTAB, TTAB and CTAB concentrations (25 mM) were used with GO and rGO to ensure that the samples remained stable for SANS. Samples with DTAB and TTAB at this concentration were regarded as metastable (Fig. 3b & c), however the sedimentation of the materials was slow enough that scattering measurements were still possible. SANS measurements from pure 25 mM solutions of DTAB, TTAB and CTAB (*i.e.* with no GO/rGO present), can be accurately modelled using an ellipsoid model<sup>66</sup> with Hayter-Penfold structure factor (Fig. 4a).<sup>67-71</sup> The fitting yields equatorial radii of 1.7, 2.0 and 2.3 nm, and axial radii of 2.7, 3.2 and 3.8 nm for DTAB, TTAB and CTAB respectively (see ESI, Table S3), concordant with literature values.<sup>72</sup> The increases in micellar radii are due to the lengths of the surfactant tails,<sup>73</sup> and the greater structure factor contributions for CTAB and TTAB (peaks at medium  $q$ ,  $0.03 \text{ \AA}^{-1}$ ) can be attributed to the larger volume fractions of micelles which will form more readily and at lower concentrations for these surfactants than DTAB (see ESI for details, Table S3).

When GO and rGO are incorporated with these surfactants (Fig. 4b & c), substantial differences in scattering in the low  $q$  region ( $0.003\text{--}0.02 \text{ \AA}^{-1}$ ) can be observed compared to the pure surfactant solutions (Fig. 4a). As  $q$  is an inverse length scale, scattering at lower  $q$  values corresponds to larger objects, which in the context of these systems must be the GO and rGO sheets. This is a very clear indication of strong interaction between the surfactant molecules and carbon nanomaterials, as the scattering from the sheets themselves was found to be negligible at  $0.1 \text{ mg/mL}$  (Fig. 1a). Furthermore, the scattering at low  $q$  conforms to a  $q^{-2}$  trend, which is indicative of scattering from flat, planar structures.<sup>74,75</sup> Note that this is not seen in the scattering of pure GO dispersions at any concentration (Fig. 2), indicating that the surfactant has changed the sheet morphology. As this trend continues even through the USANS region (Fig. 4f), it is possible that the surfactants are serving to 'flatten' the sheets and render them rigid, as crumpling of the sheets would result in an increase in the fractal dimension, and a low  $q$  slope greater than  $q^{-2}$ , as were determined in Figure 2. This phenomenon is dubbed 'nano-ironing' and could be useful in coatings or deposition applications where full exploitation of the GO and rGO surface area would be beneficial.

To model the scattering when both GO/rGO and surfactant are present, the same mass fractal model was employed to define the scattering in the low  $q$  regions.<sup>54</sup> Given that the scattering contrast in these systems is from the surfactant molecules, they will serve as the 'building blocks' for the mass fractal structure, and as their adsorption on the sheets will essentially be in a random arrangement, the mass fractal model is again an ideal representation for the GO and rGO sheet morphology. This has been used previously for similar GO/rGO systems with cationic photosurfactants.<sup>43</sup> At 25 mM however (Fig. 4b,c), the background concentration of micelles is still significant, therefore the model for the micelles must be included in the fitting algorithm to accurately fit the medium  $q$  region. Therefore the summation model method in which a step-wise addition of the fractal and micelle models was used to produce the final fits for these systems (see ESI for more detail, Fig. S7). A final

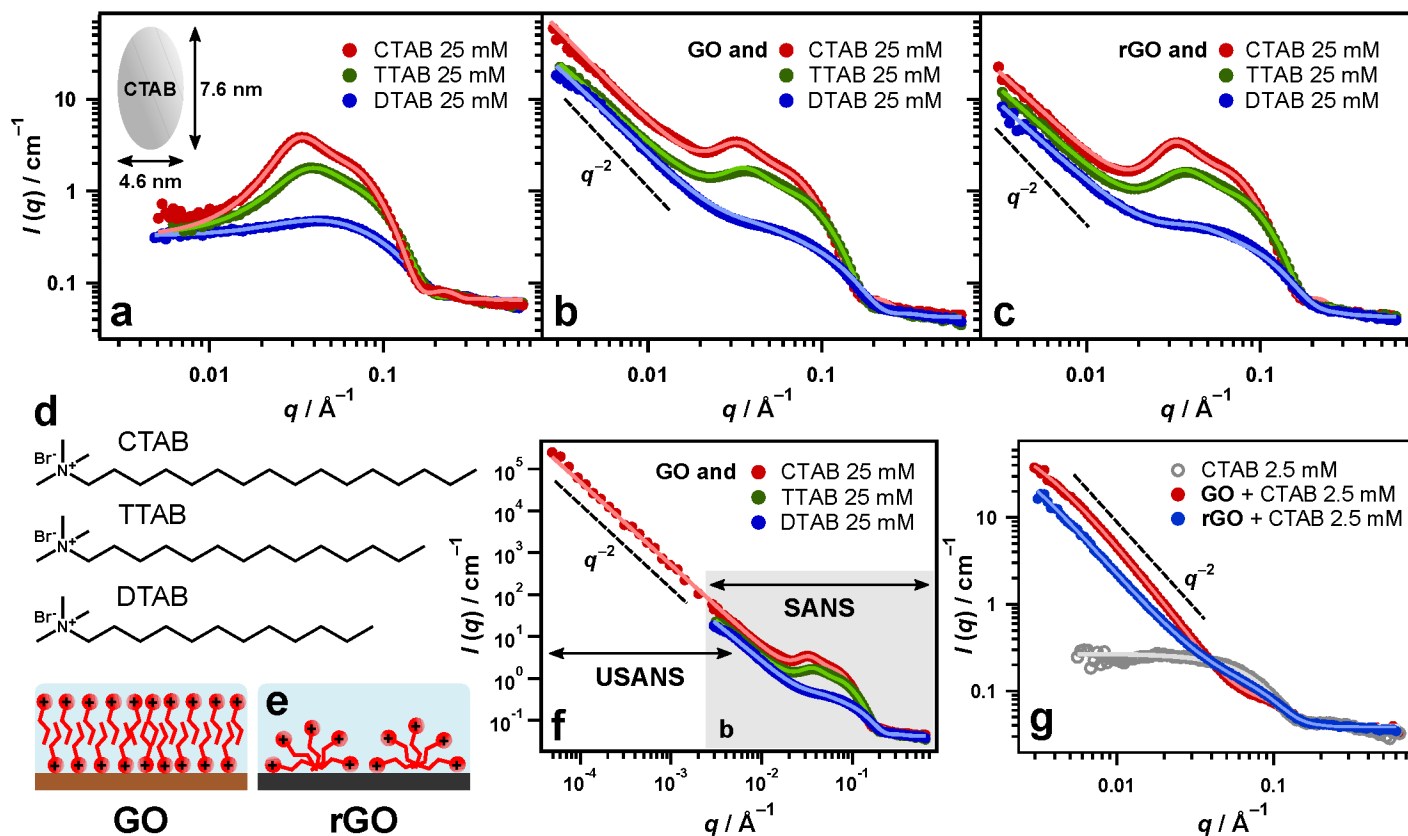


**Fig. 4** (a-c) SANS data of DTAB, TTAB and CTAB surfactants at 25 mM without carbon nanomaterial present (a), and also with GO (b) and rGO (c). Concentrations for all carbon nanomaterials were 0.1 mg/mL. The inset in (a) represents a meridional cross-section of the CTAB micelles as determined from the fitting parameters. (d) Chemical structures of DTAB, TTAB and CTAB. (e) Schematics of cationic surfactant adsorption on GO and rGO. Bromide anions have been omitted for simplicity. (f) Inclusion of USANS region to GO/CTAB data in b (shaded area). (g) SANS data of 2.5 mM CTAB with GO and rGO.

important consideration when modelling these data is the charge contribution to the scattering from the sheets themselves. As GO and rGO are highly charged, a structure factor contribution arising from interactions between sheets and micelles could be expected. However at GO and rGO concentrations of 0.1 mg/mL (0.01 wt%), the volume fraction of the sheets is so low that this effect can be regarded as negligible.

Comparing the scattering of the individual surfactants with GO and rGO, higher scattering intensities are observed in the low  $q$  region as the length of the surfactant tail is increased (Fig. 4b,c). This observation concurs with the phase behaviour in Figure 3, indicating that hydrophobicity influences the partitioning of the surfactants between the bulk aqueous phase and the sheet surfaces. Interestingly, when rGO is used, the overall scattering intensity in the fractal region is lower when compared to that of GO (Fig. 4b,c). This suggests that despite hydrophobicity of the surfactants serving to promote adsorption, a stronger affinity exists for GO than rGO, implying that electrostatic and dipole interactions are more significant for adsorption than hydrophobic interactions, as GO is more strongly charged and has a much greater proportion of oxygen-containing functional groups than rGO.<sup>5,26</sup> This may also relate to the nature of the surfactant adsorption on both carbon nanomaterials. For GO it is possible that the surfactants are adsorbing via their head-groups with

the tails protruding into solution. As this would unfavourably result in the tail-groups being exposed to the bulk aqueous solution, another monolayer of surfactants adsorbs with the head-groups now on the exterior of the structure to overcome the reorganisational entropy of water, collectively resulting in a surfactant bilayer on the surfaces of the GO sheets (Fig. 4e). Conversely for rGO, because it is hydrophobic, the surfactants most likely adsorb flat on the surfaces of the sheets, resulting in adsorbed hemispherical micelles (Fig. 4e). The adsorption mechanisms cannot be explicitly determined from the scattering data, however, the precedent for this theory has been asserted in many adsorption studies and reviews on quaternary ammonium surfactants at aqueous solid-liquid interfaces.<sup>76-80</sup> Therefore, a larger amount of surfactant molecules would be adsorbing to GO, resulting in greater scatter. The fractal dimensions for the rGO systems are also lower ( $<2$ ) than the corresponding GO samples (see ESI, Table S3), further emphasising that the interactions are weaker with rGO. It is therefore likely that GO could be superior to rGO as an aqueous adsorbent, even for certain hydrophobic materials. Similar behaviour for GO and CTAB has been predicted previously by small-angle X-ray scattering.<sup>81</sup> In all cases, the bromide counter-ions are likely to be within the vicinity of the surfactant head-groups either as undissociated moieties or as loosely bound counter-ions.<sup>82</sup> Hence, their contribution to the

assembly and thus scattering, is expected to be minimal.

Reducing the surfactant concentration to 2.5 mM, DTAB and TTAB destabilised GO and rGO, however CTAB mixtures were stable (Fig. 3b-d). At the lower concentration, the structure factor contribution from the CTAB micelles becomes negligible due to the lesser volume fraction (Fig. 4g), and they can be modelled with a simple ellipsoid model (see ESI, Table S4). Without obstruction from the large structure factor peak, the effects of the GO and rGO sheets become clearer, and it can be seen that scattering with a continuous slope of  $q^{-2}$  through medium  $q$  is apparent (Fig. 4g). The presence of the sheets results in depletion of the surfactants available for micellisation, and adsorption instead occurs along the flat, rigid GO/rGO surfaces. Again, the intensity through the low  $q$  region is higher for the GO/CTAB system than the rGO/CTAB system, showing stronger adsorption to the GO. The small shoulders around  $0.07 \text{ \AA}^{-1}$  are due to a low concentration of CTAB micelles in each mixture. Unfortunately, even at 1 mM CTAB, the presence of a non-negligible number of background micelles in the GO and rGO/CTAB mixtures means that a lamellar model could not be reliably employed to determine the thickness of the aggregates (see ESI for further explanation, Fig. S8), and the hypothesised adsorption mechanism in the two systems is therefore still only speculative at this stage.

### Interactions with anionic surfactants

Similarly to the cationic surfactants analysed, sodium dodecyl sulphate (SDS) and sodium bis(2-ethylhexyl) sulfosuccinate or Aerosol-OT (AOT) form ellipsoidal micelles, with large Hayter-Penfold structure factor peaks being caused by the overall charge of the aggregates. Hence, data for SDS and AOT were modelled similarly (see ESI). However being anionic, SDS and AOT exhibit the same surface charge as GO and rGO and hence, are likely to experience charge-based repulsions from the sheets. Modelling the SANS data for pure SDS and AOT at 25 mM (Fig. 5a) gave equatorial radii of 1.8 and 1.2 nm, and axial radii of 2.7 and 2.6 nm respectively (see ESI, Table S5), similar to literature values.<sup>83-85</sup> The shorter tail-lengths of AOT account for the lower equatorial radius of the micelles.

The equivalent SANS patterns with GO and rGO included show very little difference in the scattering to those of the blank micelles (Fig. 5b,c). Modelling these data was achieved using very similar fitting parameters (see ESI, Table S5), indicating that the micellar compositions of the samples did not notably change with the addition of GO or rGO. Therefore, little to none of the surfactant molecules are apparently adsorbed to the sheets, and are instead forming bulk micelles. The effect of same charge repulsion is likely the overriding factor dictating system behaviour here, as the surfactants could potentially adsorb to the sheets via hydrophobic interactions through their tail-groups, however the scattering suggests that the apparent adsorption is minimal, indicating that surface charge is the more dominant force. As charge interactions are longer in range,<sup>86</sup> this is to be expected. Small increases in scattering intensity are observable in the low  $q$  region for the GO and rGO samples with both surfactants (Fig. 5b,c), meaning that perhaps very small

quantities of surfactant are adsorbing. This small effect appears larger in magnitude for AOT than SDS, which could be due to AOT having a higher surface activity. Note that the scattering at low  $q$  increases appreciably for pure 25 mM AOT (Fig. 5a). The maximum aqueous solubility of AOT at room temperature is approximately 44 mM,<sup>85</sup> therefore this increase is likely due to critical scatter from inter-micellar attractions/clustering.

It is also important to note that sulfonate groups have substantial solvation shells allowing them to interact with water very strongly.<sup>87,88</sup> Therefore, SDS and AOT micelles may be further stabilised against disaggregation by their hydration from the bulk water, further inhibiting their adsorption to the GO and rGO surfaces. The lack of adsorption is thus, likely a culmination of charge repulsion and strong solvation effects. As with bromide in the case of the cationic surfactants, the dissociated sodium counter-ions are presumed to form an equilibrium between full solvation in the bulk water and weak electrostatic interactions with the SDS/AOT micelles and GO/rGO sheets. Hence, their influence in these systems is likely to be insignificant.

### Interactions with nonionic surfactants

When considering nonionic surfactants, the head-groups are uncharged, so the effects of charge-based interactions with GO and rGO become negligible. Hence, samples were found to be stable irrespective of the surfactant loadings. Triton X-100 (TX-100) is a well-known and widely utilised nonionic surfactant with a distribution of 1–20 ethylene oxide units in the head-group where the mean ethylene oxide number is 9.5, and a phenyl ring and branching in the tail-group (Fig. 6c, inset). In water at 10 mM, TX-100 forms squat cylindrical micelles (Fig. 6a) approximately 8.8 nm in length and 2.1 nm in radius (see ESI, Table S6). At the same concentration with GO and rGO present, the form factor of the TX-100 micelles is still prevalent, indicating a high presence of background micelles remaining in the system. Modelling of these systems was therefore achieved using an additive fit of cylinder and mass fractal models (see ESI). As with the cationic surfactants, an increase in scattering at low  $q$  is observed (Fig. 6b). This result can again be interpreted as surfactant adsorption to the sheets, as when reducing the concentration of TX-100 from 10 mM to 1 mM, where the micellar contribution to the scattering is significantly lower, a clear, unmasked increase in scattering intensity for the systems with GO and rGO can be seen even in the medium  $q$  region (Fig. 6c). The scattering slopes conform to  $q^{-2}$ , again indicating scattering from flat surfaces (*i.e.* the GO and rGO sheets). The trend continues into the USANS region indicating large structures, with an additional increase in slope order to  $q^{-3}$  at ultra-low  $q$ , most likely from surfactant critical scatter (Fig. 6a).

Interestingly, there are very few differences in scattering when using GO versus rGO with TX-100 (Fig. 6b,c). TX-100 has an aromatic phenyl ring, therefore it is likely to experience strong  $\pi$ -stacking interactions with rGO due to the large restoration of the aromaticity of the basal plain from the reduction process.<sup>5</sup> The  $\pi$ -stacking interactions with GO will be comparatively weak, however the polarisation interactions

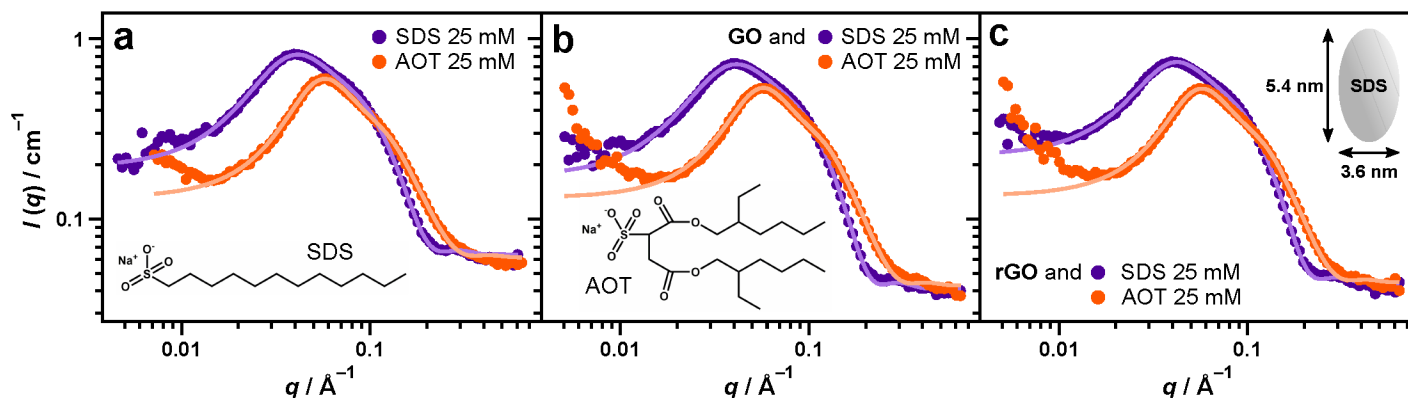


**Fig. 5** SANS data for SDS and AOT surfactants at 25 mM without carbon nanomaterial present (a) and with GO (b) and rGO (c). Concentrations for all carbon nanomaterials were 0.1 mg/mL. Insets in (a) and (b) are the chemical structures for both surfactants. The inset in (c) represents the meridional cross-section of the SDS micelles as determined from the fitting parameters.

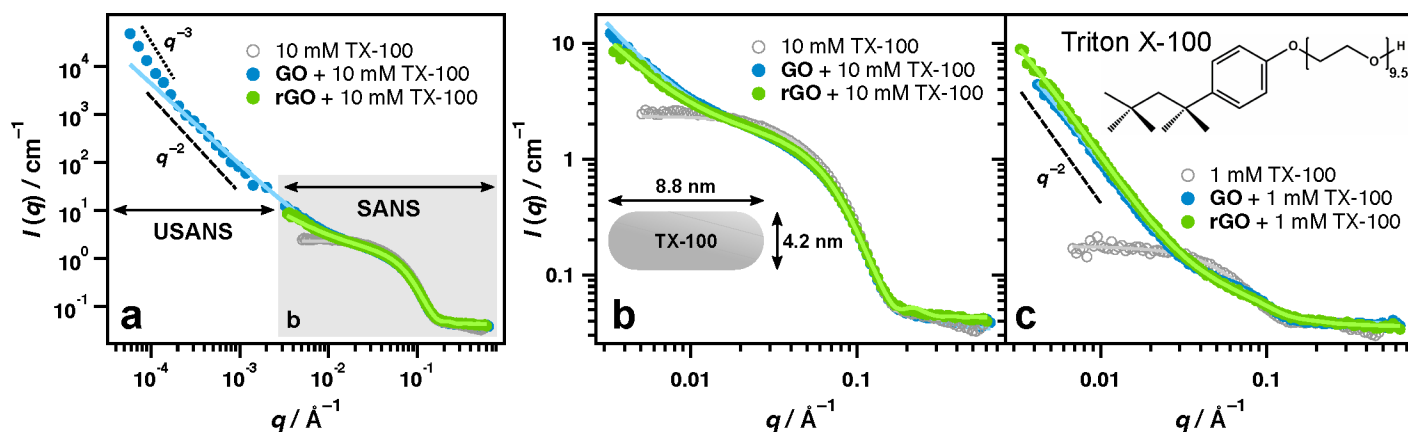


**Fig. 6** (a) SANS and USANS data of blank 10 mM TX-100 and 10 mM TX-100 with GO and rGO. (b) SANS region of the data represented by the shaded area in a. (c) Blank 1 mM TX-100 and 1 mM TX-100 with GO and rGO. The inset in (b) represents the meridional cross-section of the TX-100 cylindrical micelles as determined from the fitting parameters. Concentrations for all carbon nanomaterials were 0.1 mg/mL.

between the TX-100 head-group and GO is much stronger than for rGO. Consequently, summing the overall interactions for both materials could result in the net surfactant adsorption reaching similar levels, accounting for the lack of difference in scattering for the two materials with TX-100. It is also possible that for both materials, adsorption is dominated by head-groups interactions, and as TX-100 is polydisperse, occurs according to the preferred head-group lengths (*i.e.* molecules with shorter ethylene chains adsorb to rGO and those with longer chains adsorb to GO).

Therefore, to more systematically investigate the interactions of nonionic surfactants with GO and rGO, SANS was used to examine systems in which monodisperse  $C_nE_m$  surfactants were used. These surfactants have a specific number ( $m$ ) of ethylene oxide units for the head-group and a specific number of carbon atoms ( $n$ ) in their tail-group. For these measurements, three  $C_nE_m$  surfactants were chosen: hexaethylene glycol monododecyl ether ( $C_{12}E_6$ ), pentaethylene glycol monododecyl ether ( $C_{12}E_5$ ) and tetraethylene glycol monododecyl ether ( $C_{12}E_4$ ) (Fig. 7a). The tail-group length (12 carbons) is the same for all three molecules, however the number of ethylene glycol units varies by one, significantly altering the hydrophilicity across the series.

The most hydrophilic surfactant of this series,  $C_{12}E_6$ , was

found to form cylindrical micelles (Fig. 7b), with an average radius of 2.1 nm and length of 10.6 nm (see ESI, Table S7), concurrent with literature SANS values.<sup>89,90</sup>  $C_{12}E_5$  was found to form long, flexible cylinders (or worms) (Fig. 7c),<sup>91</sup> 2.1 nm in radius and  $C_{12}E_4$  formed vesicles (Fig. 7d),<sup>92</sup> with average radii of 25.2 nm at 10 mM and 38.3 nm at 1 mM (see ESI, Table S12). The sharper form factor resolution for  $C_{12}E_4$  at 1 mM compared to that at 10 mM is due to the difference in polydispersity for the vesicle radii of each mixture, which were 27.8 and 36.5% respectively (see ESI, Table S12). Given that the micelle morphologies and scattering intensities vary so drastically for each of these surfactants, it is difficult to draw clear distinctions between the adsorption and interactions with GO and rGO when altering the surfactant chemistry. However, for these surfactants, significant differences are evident when comparing the scattering of mixtures with GO against mixtures with rGO, an effect which was not observed for TX-100 (Fig. 6).

At 10 mM,  $C_{12}E_6$  exhibits similar scattering with GO and rGO to that of TX-100, where there appears to be a high concentration of background cylindrical micelles, and an increase in intensity at low  $q$  due to surfactant adsorbed to the sheets (Fig. 7b). However unlike TX-100, noticeably higher scattering occurs in the low  $q$

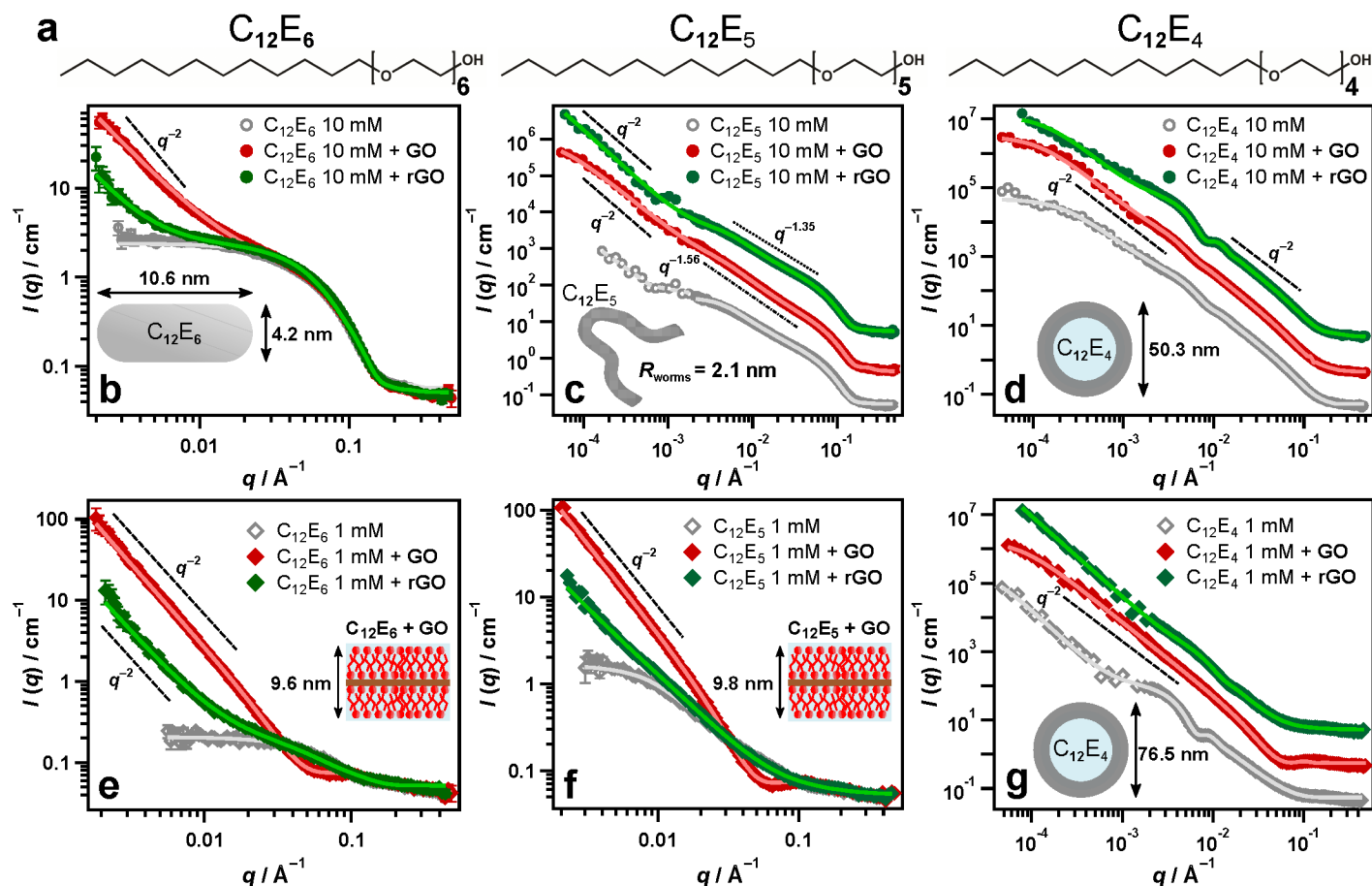


**Fig. 7** (a) Chemical structures of  $C_{12}E_6$ ,  $C_{12}E_5$  and  $C_{12}E_4$ . (b-d) SANS data of  $C_{12}E_6$ ,  $C_{12}E_5$  and  $C_{12}E_4$  surfactants (respectively) at 10 mM with and without GO and rGO (b). (e-g) SANS data of  $C_{12}E_6$ ,  $C_{12}E_5$  and  $C_{12}E_4$  surfactants (respectively) at 1 mM with and without GO and rGO (b). The data in (c), (d) and (g) include the USANS region. Concentrations for all carbon nanomaterials were 0.1 mg/mL. The insets in (b), (c), (d) and (g) represent the blank micelle structures for each surfactant as determined from the fitting parameters while the insets in (e) and (f) are schematics for the lamellar aggregates of the GO/surfactant systems as determined from the fitting. Data in figures (c), (d) and (g) have been offset by multiplication for clarity:  $\times 10$  for GO data and  $\times 100$  for rGO data.

region for the GO system than the rGO system. There is therefore a significantly greater amount of  $C_{12}E_6$  adsorbing to GO than rGO, suggesting that as with the cationic surfactants, polarisation interactions contribute more strongly to the adsorption of these molecules than do the hydrophobic (dispersion) interactions from the surfactant tail-groups. This effect would also be thermodynamically driven by freeing water entropy associated with the unfavourable solvation of hydrocarbons<sup>93,94</sup> (i.e. the surfactant tails and exclusive carbon domains of the GO and rGO, which are more substantial for rGO). Reducing the concentration of  $C_{12}E_6$  to 1 mM, the difference in scattering becomes even more marked, as the system with rGO appears to conform to the same form factor as the blank micelle sample at medium  $q$  values, whereas the system with GO has a very different shape, sharply increasing in intensity at  $q$  values below  $0.05 \text{ \AA}^{-1}$  (Fig. 7b). The low  $q$  scattering in all instances again follows a slope of  $q^{-2}$ , highlighting the flattened, sheet-like structure of the GO and rGO nanosheets. This again reinforces that the surfactants are acting to flatten the sheets, which is not observed in the naked GO and rGO dispersions (see ESI, Table S7). When using 1 mM  $C_{12}E_5$ , the overall scattering is very similar to that of  $C_{12}E_6$ , with

higher adsorption occurring on GO than rGO (Fig. 7f). Changes in hydrophobicity therefore have little impact on molecular interactions of nonionics with GO or rGO. These findings also reinforce the clear significance of the  $\pi$ -stacking interaction in the case of TX-100 with rGO. At 10 mM  $C_{12}E_5$ , the scattering from the blank micelles was so large that it obscured the data with GO and rGO, even in the low  $q$  region, hence it is difficult to draw clear conclusions from the raw scattering. However, modelling the GO and rGO systems with 10 mM  $C_{12}E_5$  revealed a steeper medium  $q$  slope for GO ( $q^{-1.56}$ ) than rGO ( $q^{-1.35}$ ). As this is the length scale in which wormlike micelles appear to be locally cylindrical ( $q^{-1}$ ),<sup>95</sup> these power laws suggest greater deviation from the wormlike structure in the GO system, which would occur if  $C_{12}E_5$  adsorption was occurring more readily to GO than rGO.

The enormous difference in surfactant adsorption on GO versus rGO can again be justified by the proposed packing mechanism for the surfactants on each surface (first described in the cationic section, Fig. 4e). As rGO represents a more hydrophobic interface, it is feasible to presume the surfactants may lie flat on the surfaces of the sheets to balance hydrophobic interactions with van der Waals forces and free water entropy.<sup>94</sup> Conversely,

because GO is predominantly hydrophilic, the surfactants are likely to be adsorbing primarily via their polar head-groups, allowing for a much denser packing arrangement in the form of surfactant bilayers.<sup>96,97</sup> This hypothesis is supported further by modelling the results for C<sub>12</sub>E<sub>6</sub> and C<sub>12</sub>E<sub>5</sub> at 1 mM with GO and rGO (see ESI, Table S8 and S11). In the cases with GO, the background micelle concentrations are clearly tiny, therefore modelling these data using exclusively a lamellar model becomes possible because there is now a well-defined upturn in the sample scattering in line with the background scattering (high  $q$ , 0.2–0.4 Å<sup>-1</sup>). The lamellar model allows determination of the average thicknesses of the aggregates based on this upturn,<sup>74</sup> which for GO/C<sub>12</sub>E<sub>6</sub> and GO/C<sub>12</sub>E<sub>5</sub> were found to be 9.6 and 9.8 nm respectively (Fig. 7e,f). These thicknesses are much greater than the 1 nm thickness for GO sheets confirmed by AFM (Fig. 1b,d), and given that the molecular length for C<sub>12</sub>E<sub>6</sub> is approximately 3.9 nm,<sup>98</sup> suggests a structure comprised of a GO sheet sandwiched between two surfactant bilayers, with significant overlap occurring between the tail-group regions (Fig. 7e,f insets). The lack of any Bragg peaks corresponding to bilayer spacings also indicates that these aggregates contain only a single sheet, and are thus, not multiply stacked. However, stacking of this nature may be possible at higher loadings of GO, and is also more credible for nonionic surfactants due to the absence of electrostatic repulsions, which would occur in the cases of the cationic surfactants. In the equivalent cases with rGO, the amount of surfactant forming micelles is apparently still too high to allow meaningful use of the lamellar model (Fig. 7e,f), and were therefore fit with additive models of micelles and mass fractals (see ESI). This also concurs with the hypothesis for surfactant adsorption mechanism, as if the surfactants adsorbed lying down on the rGO surfaces to form hemispherical micelles (Fig. 4e), the amount of surfactant adsorbed would be much lower and the scattering would be weaker, as is evident. In addition, subsequent stacking between multiple rGO sheets as is predicted for GO, would be geometrically unfavourable.

Lastly in the C<sub>*n*</sub>E<sub>*m*</sub> series, the interactions of C<sub>12</sub>E<sub>4</sub> with GO and rGO were analysed by SANS (Fig. 7d,g). C<sub>12</sub>E<sub>4</sub> is known to form large multilamellar vesicles,<sup>92,99</sup> and therefore the scattering from these mixtures was very strong, even for the pure surfactant samples. Hence, clear differences in the intensity of the scattering for these systems are difficult to interpret unambiguously. However, differences in the scattering form factors are apparent and give some physical insight into the interactions. These data, including the blank surfactants (which likely contain a mixture of vesicles, evidenced by the SANS data, and lamellae, evidenced by the USANS data),<sup>100,101</sup> were modelled using the addition of mass fractal and vesicle models (see ESI). At 10 mM C<sub>12</sub>E<sub>4</sub>, the pure surfactant solution has only a subtle vesicle form factor due to a high degree of polydispersity in the radius of the vesicles (see ESI). However, with rGO incorporated in the system, the polydispersity decreases significantly from 36.5% to 22.4%, resulting in a much sharper peak at 0.01 Å<sup>-1</sup> (Fig. 7d). This effect is interpreted as a depletion in the amount of surfactant available for micellisation due to adsorption on the rGO sheets, as decreasing the concentration of the pure C<sub>12</sub>E<sub>4</sub> solution to

1 mM also resulted in a much more well-defined vesicle form factor (Fig. 7g). For GO with C<sub>12</sub>E<sub>4</sub> at 10 mM (Fig. 7d), the co-assembly of the surfactants and sheets may also be resulting in stacked bilayers as was inferred for GO with C<sub>12</sub>E<sub>6</sub> and C<sub>12</sub>E<sub>5</sub>. In this case, the aggregates may dominate the scattering, masking the form factor for the vesicles.

At 1 mM C<sub>12</sub>E<sub>4</sub>, the clear vesicle form factor observed in the pure surfactant solution is almost totally lost when GO and rGO are added, indicating adsorption of the majority of surfactant molecules onto the sheets (Fig. 7g). However, the vesicle form factor is still slightly apparent in the rGO scattering, but not in the GO scattering, suggesting that a larger proportion of molecules are adsorbing in the case of GO. This is an interesting result, as the hydrophilicity of C<sub>12</sub>E<sub>4</sub> is significantly lower than that of C<sub>12</sub>E<sub>6</sub> and C<sub>12</sub>E<sub>5</sub>. However, the effect of dipole interactions and packing arrangement on the sheet surfaces still appear to be more significant contributors to adsorption than surfactant hydrophobicity. Scattering again conforms to a slope of  $q^{-2}$ , indicating flat surfaces (Fig. 7g). Nonionic surfactants may therefore offer useful alternatives for GO and rGO ‘nano-ironing’, as well as the spontaneous assembly of lamellar liquid crystals based on carbon nanomaterials which may be useful in optical applications and nano-templating.

### Interactions with zwitterionic surfactants

Zwitterionic surfactants also have an overall charge of zero, however unlike nonionic surfactants, there are formal charge groups associated with the surfactant heads. Erucyl amidopropyl betaine (EAPB) and oleyl amidopropyl betaine (OAPB) are environmentally friendly zwitterionic surfactants that have 22 and 18 carbons in their alkyl chains respectively (Fig. 8a).<sup>46,95</sup> These types of surfactants form complex fluids, stemming from their ability to spontaneously self-assemble into viscoelastic wormlike micelles,<sup>95</sup> and hence are commonly used in personal care products also because of their biocompatibility.<sup>102</sup> SANS data from the pure, 10 mM surfactant solutions (Fig. 8b) were thus fit using a flexible cylinder model,<sup>103,104</sup> revealing ‘worm’ radii of 2.9 and 2.2 nm for EAPB and OAPB respectively (see ESI, Table S13). The higher surface activity of EAPB from the longer tail-group results in a lower CMC, and hence, a higher volume fraction of worms compared to OAPB. Therefore, scattering intensity is greater for EAPB (Fig. 8b). Furthermore, the larger scattering volume/cross-section of the C22 chain would also significantly contribute to the greater intensity.

The one-dimensional elongation of wormlike micelles results in a low  $q$  scattering slope of  $q^{-1}$  for the pure surfactant solutions (Fig. 8b).<sup>66</sup> However, with GO and rGO added, the low  $q$  slope in all cases becomes approximately  $q^{-2}$  (Fig. 8c,d), indicating the wormlike system has evolved to a planar morphology. Therefore, as in the previous instances with cationic and nonionic surfactants, it appears that the zwitterionic betaine surfactants also have a high affinity for the sheet-like materials, and are adsorbing to the planar faces of the GO and rGO. The trend continues well into the USANS region (Fig. 8e), showing continuous aggregation of the surfactants on the surfaces of the

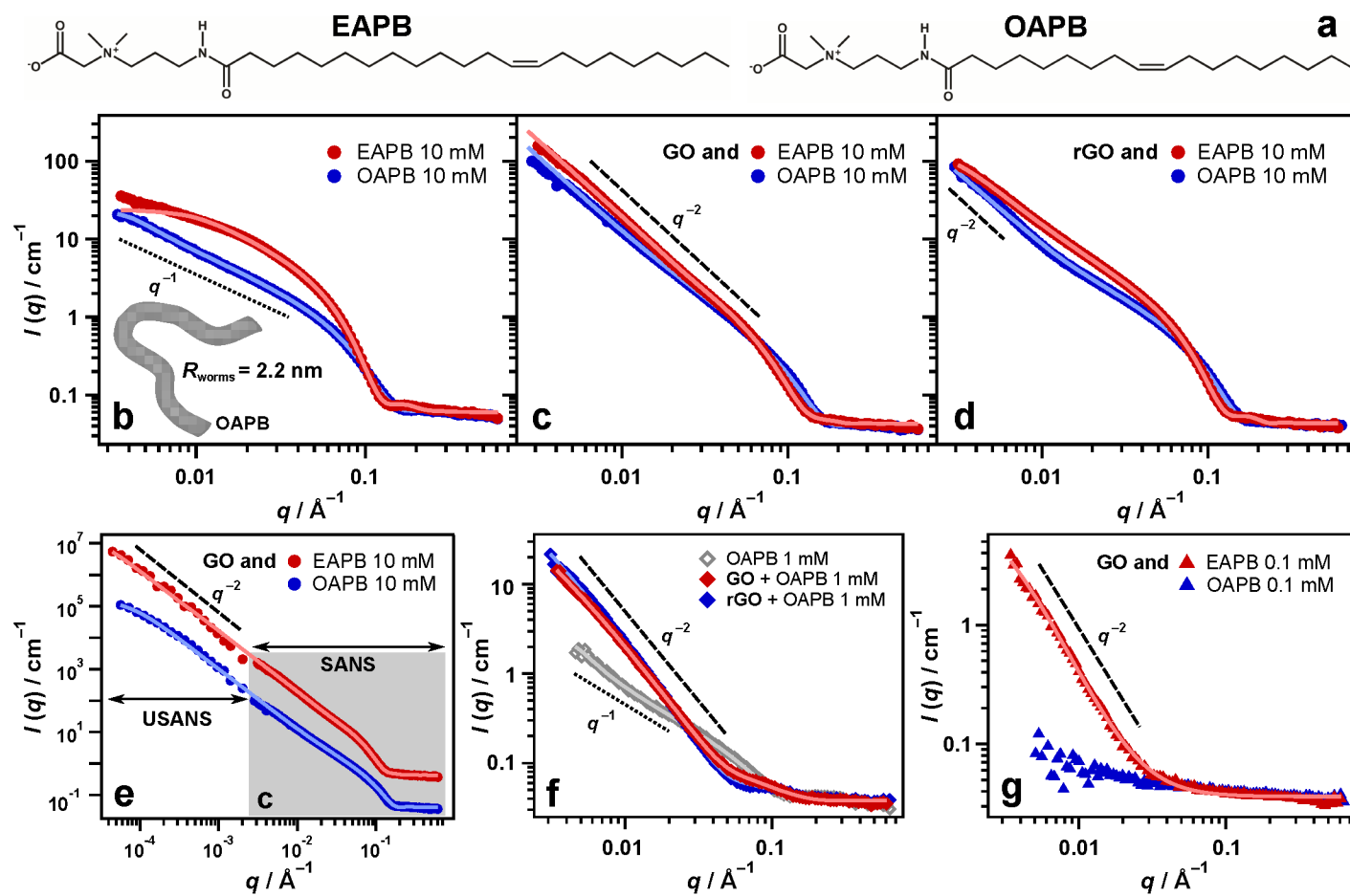


**Fig. 8** (a) Chemical structures of erucyl amidopropyl betaine (EAPB) and oleyl amidopropyl betaine (OAPB). (b-d) SANS data for EAPB and OAPB surfactants at 10 mM without carbon nanomaterial present (b), and also with GO (c) and rGO (d) at 0.1 mg/mL. The inset in (b) represents the OAPB wormlike micelles as determined by the fitting parameters. (e) Inclusion of USANS region to GO/betaine data in (c), *i.e.* the shaded area. Data in this figure have been offset by multiplication (EAPB  $\times 10$ ) for clarity (f) SANS data of pure 1 mM OAPB, and also with GO and rGO present at 0.1 mg/mL. (g) SANS data of GO with 0.1 mM EAPB and OAPB.

sheets. At 10 mM EAPB and OAPB, for both GO and rGO, the adsorption appears to be slightly stronger for EAPB than OAPB. This is likely due to the higher surface activity of EAPB causing it to partition more to the interface with GO and rGO, however the difference is only minor and likely also relates to the scattering length densities of the surfactants, which will be lower for EAPB, giving higher contrast with  $\text{D}_2\text{O}$  (neutron scattering length densities for protium *ca.*  $-3.74$  and deuterium *ca.*  $6.67 \times 10^{-6} \text{ \AA}^{-2}$ ).

Moreover, the differences in the scattering of GO and rGO with both surfactants seem insignificant (Fig. 8c,d). The likely explanation for the lack of difference for the two materials may reside in the chemical complexity of these particular surfactants as well as the fact that the extra long tail-groups render them very hydrophobic. Being zwitterionic, the effects of the charge groups become reduced due to self-screening, however they, along with the amide group further towards the center of the molecule (Fig. 8a), will still experience strong polar interactions with their surroundings. In addition, these surfactants have an unsaturated group in their alkyl tails, meaning that similar to TX-100,  $\pi$ -stacking interactions may also contribute. Coupling

the  $\pi$ -stacking interactions with the long 18 and 22 carbon tail-groups, these molecules will exhibit much stronger hydrophobic interactions than the previous surfactants examined. Therefore overall, the attractive forces arising from both the dipole and very strong hydrophobic interactions are most likely going to mean that surfactant-surfactant interactions dominate in the case of these long-chain betaines.<sup>105,106</sup> Hence, these surfactants readily form bilayers and can be considered lipid-like molecules. As a result, these surfactants are likely to form bilayers on both GO and rGO irrespective of their chemical nature because of overriding surfactant-surfactant interactions.

When reducing the concentration of OAPB to 1 mM, differences in the amount of scattering when mixed with GO and rGO were also negligible (Fig. 8f). As one might expect the partitioning between bulk and adsorbed surfactant to be different at lower concentrations, this outcome reinforces the hypothesis that for these lipid-like surfactants, intermolecular interactions between surfactant molecules are likely dominating. Bilayer formation on the GO and rGO surfaces is thus the favourable adsorption assembly, and therefore the effects of the carbon nanomaterials become less significant. Equivalent samples with EAPB at 1 mM

were unstable, possibly because at this concentration the amount of surfactant is not enough to form bilayers on the sheets, and they instead become hydrophobic, resulting in aggregation. Hence, these samples were not amenable to analysis with SANS. A comparison between the two surfactants could however be made when reducing the surfactant concentration to 0.1 mM (Fig. 8g). The scattering with GO was found to be substantially stronger for EAPB than OAPB, showing that hydrophobicity does have a notable contribution to the interactions and adsorption of small molecules with these carbon nanomaterials.

### Interactions with polymers

Block co-polymers have been used with GO to enhance surface activity,<sup>107,108</sup> as well as assist with dispersion of carbon nanotubes.<sup>109,110</sup> For the final additive class of this study, the interactions of two model polymers with aqueous dispersions of GO and rGO were explored using SANS. Two common polymers were chosen: polyethylene glycol (PEG) and Pluronic F127, which is a widely used triblock co-polymer (structures shown in Fig. 9a). Dispersed in water on their own, PEG and Pluronic F127 give fairly weak scattering, however the scattering of PEG is stronger than the scattering of Pluronic F127 (Fig. 9a). The reason behind this result is that the PEG chains are much larger, and in solution follow an essentially 'random walk' or Gaussian coil,<sup>111</sup> whereas Pluronic F127 self-assembles into loosely aggregated, highly hydrated spherical micelles.<sup>112,113</sup> These patterns were fit with unified power models to determine their radii of gyration (for polymers, this relates to the interactions between chains and monomers as well as size),<sup>114,115</sup> which were 22.2 and 4.0 nm for PEG and Pluronic F127 respectively (see ESI, Table S14), indicating that PEG units are more dispersed with longer contour lengths. Both polymers are intrinsically hydrophilic, however Pluronic F127 is also amphiphilic because of its methylated central block, driving micellisation. Therefore, the scattering data for Pluronic F127 in Figure 9a can also be fit with a spheres model (see ESI, Fig. S11),<sup>116</sup> revealing spherical micelles of approximately 4.0 nm in radius (see ESI, Table S15), the same as the radius of gyration, which is to be expected for spheres.

For both polymers, the scattering intensities increased with the inclusion of GO and rGO. This increase was only very slight with GO (Fig. 9b), indicating minimal interactions between the materials. However contrary to any of the surfactant systems, both polymers displayed a significantly higher affinity for rGO (Fig. 9c). The unified power model also gives good approximation for the scattering from fractal aggregates (such as GO and rGO sheets),<sup>111</sup> therefore is also valid for the combined polymer/GO and rGO systems. The radius of gyration for PEG and Pluronic F127 with rGO increased to 36.3 and 26.7 nm respectively (see ESI, Table S14), which translates to a 567.5% increase for Pluronic F127. Pluronic F127 is therefore most likely changing from spherical micelles in the pure polymer solution to unravelled, adsorbed polymer chains on the surfaces of the sheets. These effects are most likely thermodynamically driven, and can be explained by the solvation of these materials by water

molecules. As both polymers are hydrophilic and GO is also hydrophilic, there is little entropic gain in their co-assembly with regards to the solvent water molecules, as both the polymers and GO have favourable polar interaction sites with which water can interact. Therefore the materials will mostly remain solvated in the bulk rather than adsorbing to each other. However, because rGO is hydrophobic, the adsorption of the polymers (especially Pluronic F127) will serve to free water molecules that are unfavourably oriented at the interfaces with the rGO sheets.<sup>117</sup> This outcome would correspond to an increase in entropy, and hence would be thermodynamically favoured. The adsorption of the polymer onto rGO is thus greater, accounting for the higher scattering of the rGO/polymer systems compared to the GO/polymer systems.

To corroborate the scattering data and the conclusions drawn from them, atomic force microscopy (AFM) imaging was performed on these systems to see if physical evidence for the adsorption of the polymers could be observed. Without GO or rGO added, PEG appeared to form small aggregates when dried onto the surface of mica, whereas Pluronic F127 appeared to spread over the mica surface (Fig. 10a,d). These results suggest a higher adsorption affinity for Pluronic F127 than PEG on mica. With GO and rGO added, the deposited materials do appear to show adsorbed polymer on the surfaces of the sheets (Fig. 10b,c,e,f). In the samples with rGO, almost all of the polymer material appears to be co-located on to the sheets rather than the background mica (Fig. 10c,f), reasserting the strong co-assembly indicated by the scattering with rGO and both polymers (Fig. 9c). While some polymer adsorption is evident for the samples with GO, the effect is not quite as clear, especially in the case of Pluronic F127 (Fig. 10b,e), again supporting the scattering data (Fig. 9b). When increasing the amount of polymer in these mixtures by a factor of 5 and again imaging by AFM, it was found that the addition of rGO completely disrupted the fractal aggregation exhibited by the pure polymers at this loading, whereas GO caused only partially disrupted aggregation (see ESI, Table S14). This again indicates stronger interactions with rGO than GO, and suggests that the design of composite materials comprising polymers and carbon nanomaterials may be more effective when rGO is used. It must be noted that as these are dried samples, they are only indicative of the solution behaviour and must be interpreted with caution.

## 4 Conclusions

A range of surfactants that were systematically varied in specific physical properties such as charge and hydrophobicity were added to aqueous dispersions of monolayer graphene oxide (GO) and reduced graphene oxide (rGO). Small and ultra-small-angle neutron scattering (SANS and USANS) was used to monitor the self-assembly within these systems, giving insight into the adsorption and interactions between the surfactants and carbon nanomaterials. Electrostatic interactions were found to be the most dominant forces in these systems, as cationic surfactants showed very high affinity for GO and rGO, whereas anionic surfactants exhibited almost no adsorption. Nonionic and zwitterionic surfactants also adsorbed strongly to both materials,

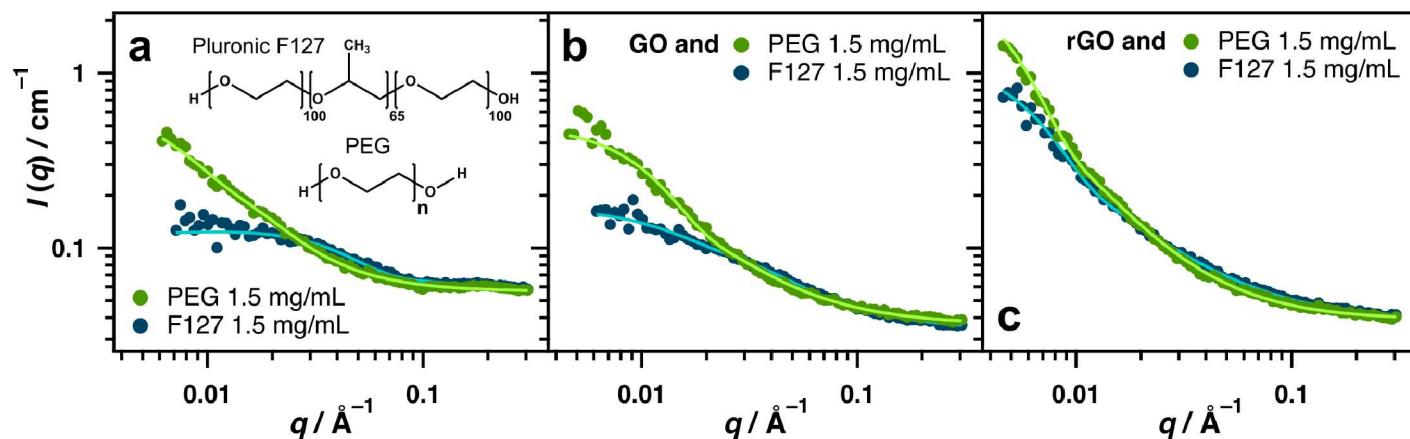


Fig. 9 SANS data for PEG (M<sub>v</sub> = 400,000 g/mol) and Pluronic F127 at 1.5 mg/mL without carbon nanomaterial present (a) and with GO (b) and rGO (c). Concentrations for all carbon nanomaterials were 0.1 mg/mL. Insets to (a) are chemical structures of each polymer.

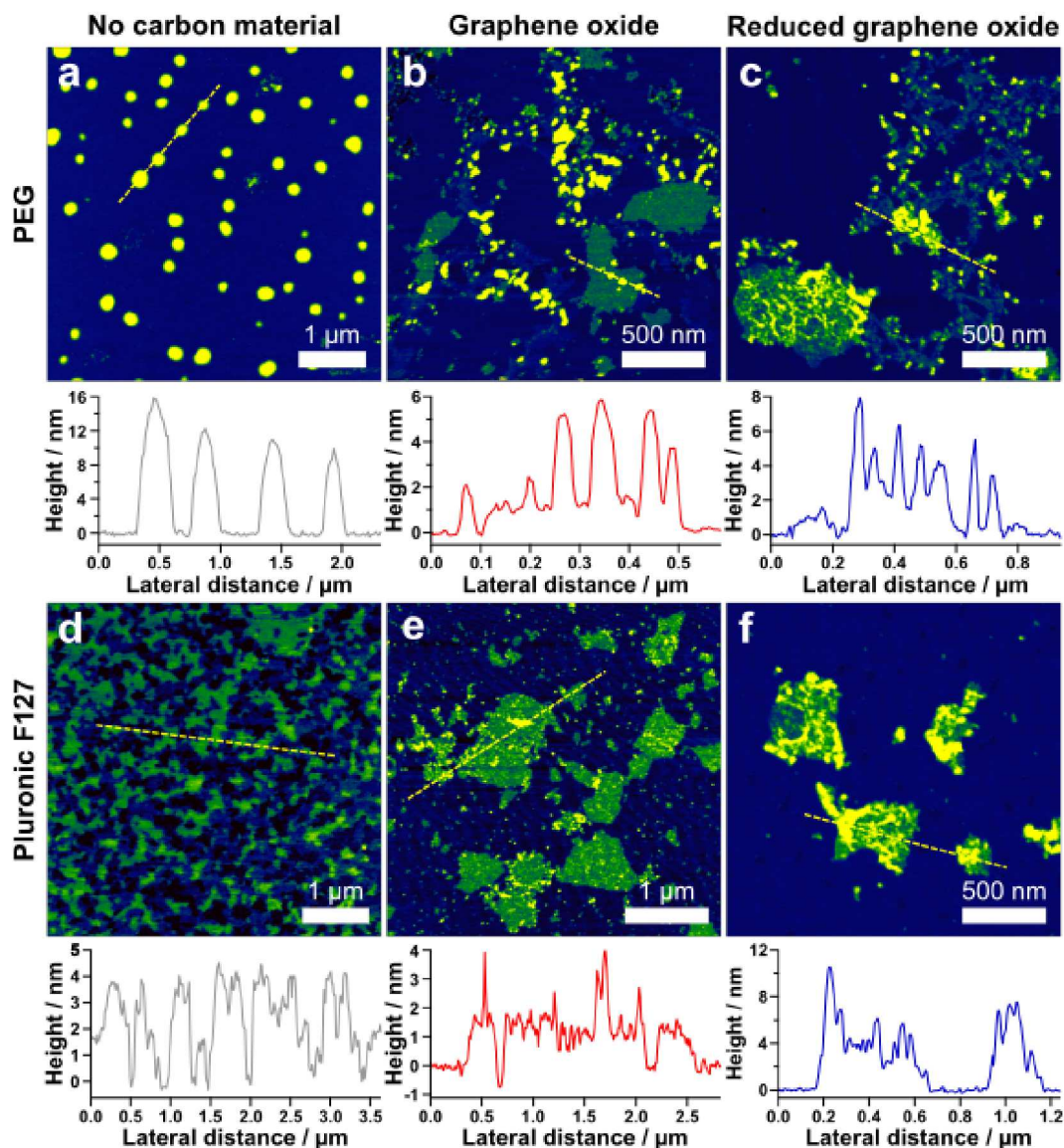


Fig. 10 AFM images of 0.1 mg/mL of polymer with or without 0.1 mg/mL GO or rGO in dispersion: (a-c) AFM height images of PEG (a) with GO (b) and rGO (c). (d-f) AFM height images of pluronic F127 (d) with GO (e) and rGO (f). Height profiles corresponding to the dashed yellow cross sections are shown below each respective image. Samples were dried onto mica substrate.

suggesting however that charge is not the sole factor driving adsorption, and that dipole and hydrophobic interactions are also strong contributors to their assembly. Lastly, two neutral polymers, one of which was completely hydrophilic and the other amphiphilic, were mixed with GO and rGO, both showing moderate or weak interactions that were apparently entropic in origin as evidenced by higher adsorption to rGO than GO. This indicates that additives do not have to be amphiphilic in order to adsorb to aqueous carbon nanomaterials, and in certain circumstances is thermodynamically driven.

Interestingly, when comparing the behaviour of GO and rGO, in most cases, greater scattering was evident in systems with GO, indicating higher levels of adsorption. This suggests that dipole interactions are typically more significant than hydrophobic effects with relation to adsorption of amphiphiles on these materials. To account for this observation, we propose a differing adsorption mechanism for surfactants on GO versus rGO. With GO, we believe that surfactants are adsorbing via their head-groups due to the stronger dipole interactions, and as a result, form a densely packed surfactant bilayer along the surface of the GO sheets. This structure is clearly apparent when using nonionic surfactants, and these bilayers could then stack with multiple sheets to form lamellae (liquid crystals) due to the absence of charge repulsion between surfactant layers. For rGO however, because the sheets are inherently more hydrophobic, the surfactants are more likely to lie flat on the surface because of stronger hydrophobic interactions (*i.e.* entropic effects arising from water structuring),<sup>94</sup> resulting in hemispherical micelles.<sup>78,79</sup> Thus, the amount of surfactant adsorbed to GO is greater due to the denser packing arrangement. Surfactants that were more hydrophobic also appeared to adsorb more readily than equivalent surfactants with shorter tail-groups, presumably due to increased surface active partitioning.

Where surfactant adsorption was evident, the scattering at low  $q$  (the fractal region) often followed a trend of  $q^{-2}$ , indicating scattering from flat surfaces. The surfactants therefore were effectively flattening the GO and rGO sheets in solution (nanorolling). Hence, these composite systems could also be useful in materials coatings where the surfactants serve to maximise the carbon nanomaterial surface area. The overall results collectively provide a broader understanding of the nature of molecular interactions with aqueous GO and rGO nanosheets, and may assist with the effective utilisation of these materials in adsorption, stabilisation and environmental applications where synergism can be used to enhance effectiveness and develop new routes to diverse, chemically functional systems.

## Conflicts of interest

There are no conflicts to declare.

## Acknowledgements

We would like to acknowledge the Australian Centre for Neutron Scattering, Australian Nuclear Science and Technology Organisation, for beam-time. We also thank the Australian Institute of Nuclear Science and Engineering for travel support (T.M.M), as well as the Monash Centre for Atomically Thin

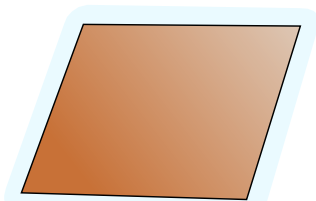
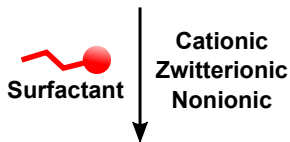
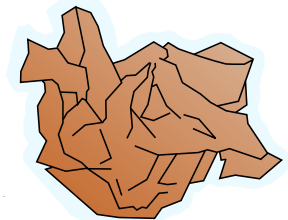
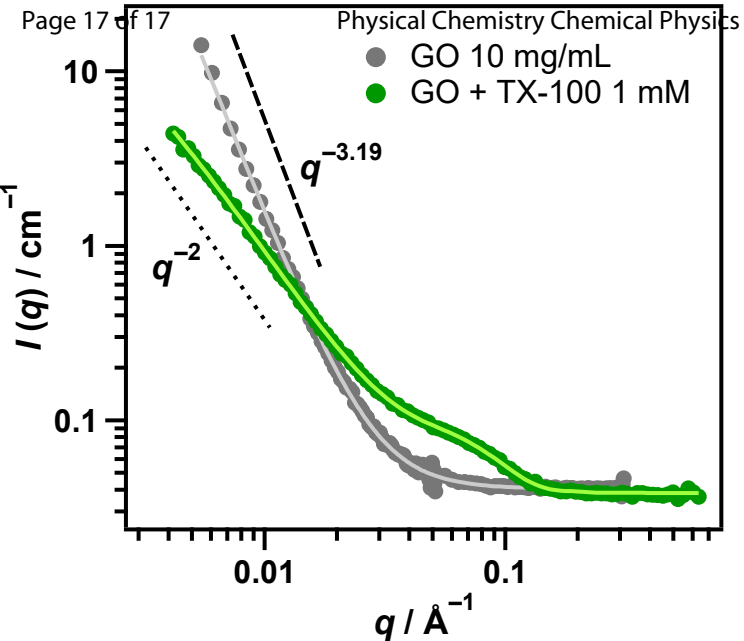
Materials for additional funding. This work was supported in part by the grant of an ARC Future Fellowship (FT160100191) to R.F.T. We would lastly like to thank Gregory Warr, Yachin Cohen and Stuart Prescott for insightful discussions on scattering phenomena.

## Notes and references

- 1 K. S. Novoselov, A. K. Geim, S. V. Morozov, D. Jiang, Y. Zhang, S. V. Dubonos, I. V. Grigorieva and A. A. Firsov, *Science*, 2004, **306**, 666–669.
- 2 J. C. Meyer, A. K. Geim, M. I. Katsnelson, K. S. Novoselov, T. J. Booth and S. Roth, *Nature*, 2007, **446**, 60.
- 3 D. R. Dreyer, S. Park, C. Bielawski and R. S. Ruoff, *Chem. Soc. Rev.*, 2010, **39**, 228–240.
- 4 S. Stankovich, D. A. Dikin, R. D. Piner, K. A. Kohlhaas, A. Kleinhammes, Y. Jia, Y. Wu, S. T. Nguyen and R. S. Ruoff, *Carbon*, 2007, **45**, 1558–1565.
- 5 D. Li, M. B. Muller, S. Gilje, R. B. Kaner and G. G. Wallace, *Nat. Nanotechnol.*, 2008, **3**, 101–105.
- 6 G. K. Ramesha, A. V. Kumara, H. B. Muralidhara and S. Sampath, *J. Colloid Interface Sci.*, 2011, **361**, 270–277.
- 7 G. Zhao, J. Li, X. Ren, C. Chen and X. Wang, *Environ. Sci. Technol.*, 2011, **45**, 10454–10462.
- 8 K. Gupta and O. P. Khatri, *Journal of colloid and interface science*, 2017, **501**, 11–21.
- 9 J. Kim, L. J. Cote, W. Kim, F. Yuan, K. R. Shull and J. Huang, *J. Am. Chem. Soc.*, 2010, **132**, 8180–8186.
- 10 Y. He, F. Wu, X. Sun, R. Li, Y. Guo, C. Li, L. Zhang, F. Xing, W. Wang and J. Gao, *ACS Appl. Mater. Interfaces*, 2013, **5**, 4843–4855.
- 11 T. M. McCoy, M. J. Pottage and R. F. Tabor, *J. Phys. Chem. C*, 2014, **118**, 4529–4535.
- 12 Y. He, N. Zhang, F. Wu, F. Xu, Y. Liu and J. Gao, *Mater. Res. Bull.*, 2013, **48**, 3553 – 3558.
- 13 Y. Lei, F. Chen, Y. Luo and L. Zhang, *Chem. Phys. Lett.*, 2014, **593**, 122 – 127.
- 14 Z. Niu, J. Chen, H. H. Hng, J. Ma and X. Chen, *Adv. Mater.*, 2012, **24**, 4144–4150.
- 15 Y. He, Y. Liu, T. Wu, J. Ma, X. Wang, Q. Gong, W. Kong, F. Xing, Y. Liu and J. Gao, *J. Hazard. Mater.*, 2013, **260**, 796–805.
- 16 D. A. Dikin, S. Stankovich, E. J. Zimney, R. D. Piner, G. H. B. Dommett, G. Evmenenko, S. T. Nguyen and R. S. Ruoff, *Nature Letters*, 2007, **448**, 457–460.
- 17 Y. Su, V. Kravets, S. Wong, J. Waters, A. Geim and R. Nair, *Nat. Commun.*, 2014, **5**, 4843.
- 18 J. Hong, Y. S. Kang and S. W. Kang, *Ind. Eng. Chem. Res.*, 2011, **50**, 3095–3099.
- 19 F. Kim, L. J. Cote and J. Huang, *Adv. Mater.*, 2010, **22**, 1954–1958.
- 20 L. J. Cote, J. Kim, Z. Zhang, C. Sun and J. Huang, *Soft Matter*, 2010, **6**, 6096–6101.
- 21 M. Krueger, S. Berg, D. Stone, E. Strelcov, D. A. Dikin, J. Kim, L. J. Cote, J. Huang and A. Kolmakov, *ACS Nano*, 2011, **5**,

- 10047–10054.
- 22 G. Z. Kyzas, E. A. Deliyanni and K. A. Matis, *J. Chem. Technol. Biotechnol.*, 2014, **89**, 196–205.
- 23 H. Bai, C. Li, X. Wang and G. Shi, *J. Phys. Chem. C*, 2011, **115**, 5545–5551.
- 24 A. Akbari, P. Sheath, S. T. Martin, D. B. Shinde, M. Shaibani, P. C. Banerjee, R. Tkacz, D. Bhattacharyya and M. Majumder, *Nature communications*, 2016, **7**, 10891.
- 25 D. C. Marcano, D. V. Kosynkin, J. M. Berlin, A. Sinitskii, Z. Sun, A. Slesarev, L. B. Alemany, W. Lu and J. M. Tour, *ACS Nano*, 2010, **4**, 4806–4814.
- 26 B. Konkena and S. Vasudevan, *J. Phys. Chem. Lett.*, 2012, **3**, 867–872.
- 27 C.-J. Shih, S. Lin, R. Sharma, M. S. Strano and D. Blankschtein, *Langmuir*, 2012, **28**, 235–241.
- 28 T. D. Gamot, A. R. Bhattacharyya, T. Sridhar, F. Beach, R. F. Tabor and M. Majumder, *Langmuir*, 2017, **33**, 10311–10321.
- 29 I. Chowdhury, N. D. Mansukhani, L. M. Guiney, M. C. Hersam and D. Bouchard, *Environ. Sci. Technol.*, 2015, **49**, 10886–10893.
- 30 D. Kang, J. Y. Kwon, H. Cho, J.-H. Sim, H. S. Hwang, C. S. Kim, Y. J. Kim, R. S. Ruoff and H. S. Shin, *ACS Nano*, 2012, **6**, 7763–7769.
- 31 F. A. Ghauri, M. A. Raza, M. S. Baig and S. Ibrahim, *Mater. Res. Exp.*, 2017, **4**, 125601.
- 32 L. L. Zhang, X. Zhao, M. D. Stoller, Y. Zhu, H. Ji, S. Murali, Y. Wu, S. Perales, B. Clevenger and R. S. Ruoff, *Nano Lett.*, 2012, **12**, 1806–1812.
- 33 Y. Chen, X. Zhang, D. Zhang, P. Yu and Y. Ma, *Carbon*, 2011, **49**, 573–580.
- 34 X. Zhu, Y. Zhu, S. Murali, M. D. Stoller and R. S. Ruoff, *ACS Nano*, 2011, **5**, 3333–3338.
- 35 B. Qu, C. Ma, G. Ji, C. Xu, J. Xu, Y. S. Meng, T. Wang and J. Y. Lee, *Adv. Mater.*, 2014, **26**, 3854–3859.
- 36 N. Li, M. Zheng, H. Lu, Z. Hu, C. Shen, X. Chang, G. Ji, J. Cao and Y. Shi, *Chem. Comm.*, 2012, **48**, 4106–4108.
- 37 B. Wang, X. Li, X. Zhang, B. Luo, M. Jin, M. Liang, S. A. Dayeh, S. Picraux and L. Zhi, *ACS Nano*, 2013, **7**, 1437–1445.
- 38 L. J. Cote, J. Kim, V. C. Tung, J. Luo, F. Kim and J. Huang, *Pure Appl. Chem.*, 2010, **83**, 95–110.
- 39 N. Lu and Z. Li, in *Quantum Simulations of Materials and Biological Systems*, Springer, 2012, ch. Graphene Oxide: Theoretical Perspectives, pp. 69–84.
- 40 N. Wei, C. Lv and Z. Xu, *Langmuir*, 2014, **30**, 3572–3578.
- 41 M. Zokaie and M. Foroutan, *RSC Adv.*, 2015, **5**, 39330–39341.
- 42 H. Tang, D. Liu, Y. Zhao, X. Yang, J. Lu and F. Cui, *J. Phys. Chem. C*, 2015, **119**, 26712–26718.
- 43 T. M. McCoy, A. C. Y. Liu and R. F. Tabor, *Nanoscale*, 2016, **8**, 6969–6974.
- 44 D. Feng, Y. Zhang, Q. Chen, J. Wang, B. Li and Y. Feng, *J. Surfactants Deterg.*, 2012, **15**, 657–661.
- 45 G. A. Gaynanova, A. R. Valiakhmetova, D. A. Kuryashov, N. Y. Bashkirtseva and L. Y. Zakharova, *J. Surfactants Deterg.*, 2015, **18**, 965–971.
- 46 V. T. Kelleppan, J. E. Moore, T. M. McCoy, A. V. Sokolova, L. d. Campo, B. L. Wilkinson and R. F. Tabor, *Langmuir*, 2017, **34**, 970–977.
- 47 A. Sokolova, J. Christoforidis, A. Eltobaji, J. Barnes, F. Darmann, A. E. Whitten and L. de Campo, *Neutron News*, 2016, **27**, 9–13.
- 48 C. Rehm, A. Brùlé, A. K. Freund and S. J. Kennedy, *J. Appl. Crystallogr.*, 2013, **46**, 1699–1704.
- 49 C. Rehm and L. de Campo, *Neutron News*, 2016, **27**, 30–32.
- 50 C. Rehm, L. d. Campo, A. Brùlé, F. Darmann, F. Bartsch and A. Berry, *J. Appl. Crystallogr.*, 2018, **51**, year.
- 51 S. R. Kline, *J. Appl. Crystallogr.*, 2006, **39**, 895–900.
- 52 D. Nečas and P. Klapetek, *Open Physics*, 2012, **10**, 181–188.
- 53 G. Titelman, V. Gelman, S. Bron, R. Khalfin, Y. Cohen and H. Bianco-Peled, *Carbon*, 2005, **43**, 641–649.
- 54 D. F. R. Mildner and P. L. Hall, *J. Phys. D: Appl. Phys.*, 1986, **19**, 1535–1545.
- 55 G. Bushell, Y. Yan, D. Woodfield, J. Raper and R. Amal, *Adv. Colloid Interface Sci.*, 2002, **95**, 1–50.
- 56 J. D. Ramsay, S. W. Swanton and J. Bunce, *J. Chem. Soc., Faraday Trans.*, 1990, **86**, 3919–3926.
- 57 P. W. Schmidt, *J. Appl. Crystallogr.*, 1991, **24**, 414–435.
- 58 A. Y. Cherny, E. Anitas, V. Osipov and A. Kuklin, *J. Appl. Crystallogr.*, 2014, **47**, 198–206.
- 59 T. M. McCoy, P. Brown, J. Eastoe and R. F. Tabor, *ACS Appl. Mater. Interfaces*, 2015, **7**, 2124–2133.
- 60 H. Kim, Y. R. Jang, J. Yoo, Y.-S. Seo, K.-Y. Kim, J.-S. Lee, S.-D. Park, C.-J. Kim and J. Koo, *Langmuir*, 2014, **30**, 2170–2177.
- 61 T. M. McCoy, S. A. Holt, A. M. Rozario, T. D. M. Bell and R. F. Tabor, *Adv. Mater. Interfaces*, 2017, **4**, 1700803–n/a.
- 62 M. Abdolkarimi-Mahabadi and M. Manteghian, *J. Dispersion Sci. Technol.*, 2015, **36**, 924–931.
- 63 T. M. McCoy, H. C. W. Parks and R. F. Tabor, *Carbon*, 2018, **135**, 164–170.
- 64 S. P. Moulik, M. E. Haque, P. K. Jana and A. R. Das, *J. Phys. Chem.*, 1996, **100**, 701–708.
- 65 Z. Adamczyk, G. Para and P. Warszyński, *Langmuir*, 1999, **15**, 8383–8387.
- 66 L. Feigin, D. I. Svergun and G. W. Taylor, *Structure analysis by small-angle X-ray and neutron scattering*, Springer, 1987, pp. 25–55.
- 67 J. B. Hayter and J. Penfold, *Mol. Phys.*, 1981, **42**, 109–118.
- 68 J. B. Hayter and J. Penfold, *J. Chem. Soc., Faraday Trans. I*, 1981, **77**, 1851–1863.
- 69 J.-P. Hansen and J. B. Hayter, *Molecular Physics*, 1982, **46**, 651–656.
- 70 J. B. Hayter and J. Penfold, *Colloid Polym. Sci.*, 1983, **261**, 1022–1030.
- 71 C. Wu, D. Y. Chan and R. F. Tabor, *J. Colloid Interface Sci.*, 2014, **426**, 80–82.
- 72 V. Aswal and P. Goyal, *Physica B*, 1998, **245**, 73–80.

- 73 S. Berr, *J. Phys. Chem.*, 1987, **91**, 4760–4765.
- 74 J. Berghausen, J. Zipfel, P. Lindner and W. Richtering, *J. Phys. Chem. B*, 2001, **105**, 11081–11088.
- 75 N. Kučerka, J. F. Nagle, J. N. Sachs, S. E. Feller, J. Pencer, A. Jackson and J. Katsaras, *Biophys. J.*, 2008, **95**, 2356–2367.
- 76 P. Somasundaran, T. W. Healy and D. Fuerstenau, *J. Phys. Chem.*, 1964, **68**, 3562–3566.
- 77 S. Manne and H. E. Gaub, *Science*, 1995, **270**, 1480–1482.
- 78 G. G. Warr, *Curr. Opin. Colloid Interface Sci.*, 2000, **5**, 88–94.
- 79 R. Atkin, V. Craig, E. J. Wanless and S. Biggs, *Adv. Colloid Interface Sci.*, 2003, **103**, 219–304.
- 80 R. Atkin, V. Craig and S. Biggs, *Langmuir*, 2000, **16**, 9374–9380.
- 81 W. Meng, E. Gall, F. Ke, Z. Zeng, B. Kopchick, R. Timsina and X. Qiu, *J. Phys. Chem. C*, 2015, **119**, 21135–21140.
- 82 K. Eskilsson and V. Yaminsky, *Langmuir*, 1998, **14**, 2444–2450.
- 83 S. Hayashi and S. Ikeda, *J. Phys. Chem.*, 1980, **84**, 744–751.
- 84 M. Bergstrom and J. S. Pedersen, *Phys. Chem. Chem. Phys.*, 1999, **1**, 4437–4446.
- 85 S. Nave, J. Eastoe, R. K. Heenan, D. Steytler and I. Grillo, *Langmuir*, 2000, **16**, 8741–8748.
- 86 S. Bhatia, J. Barker and A. Mourchid, *Langmuir*, 2003, **19**, 532–535.
- 87 K. A. Mauritz and R. B. Moore, *Chem. Rev.*, 2004, **104**, 4535–4586.
- 88 Q. Zhao, P. Majsztrik and J. Benziger, *J. Phys. Chem. B*, 2011, **115**, 2717–2727.
- 89 R. Zielinski, E. Kaler and M. Paulaitis, *J. Phys. Chem.*, 1995, **99**, 10354–10358.
- 90 J. Gapinski, J. Szymanski, A. Wilk, J. Kohlbrecher, A. Patkowski and R. Hołyst, *Langmuir*, 2010, **26**, 9304–9314.
- 91 A. Bernheim-Groswasser, E. Wachtel and Y. Talmon, *Langmuir*, 2000, **16**, 4131–4140.
- 92 F. Nettesheim, J. Zipfel, P. Lindner and W. Richtering, *Coll. Surf. A*, 2001, **183-185**, 563–574.
- 93 B.-Y. Zhu and T. Gu, *Adv. Colloid Interface Sci.*, 1991, **37**, 1–32.
- 94 R. F. Tabor, F. Grieser, R. R. Dagastine and D. Y. C. Chan, *Phys. Chem. Chem. Phys.*, 2014, **16**, 18065–18075.
- 95 T. M. McCoy, A. Valiakhmetova, M. J. Pottage, C. J. Garvey, L. de Campo, C. Rehm, D. A. Kuryashov and R. F. Tabor, *Langmuir*, 2016, **32**, 12423–12433.
- 96 F. Tiberg, J. Brinck and L. Grant, *Curr. Opin. Colloid Interface Sci.*, 1999, **4**, 411–419.
- 97 R. Zhang and P. Somasundaran, *Adv. Colloid Interface Sci.*, 2006, **123**, 213–229.
- 98 W. Brown, R. Johnsen, P. Stilbs and B. Lindman, *J. Phys. Chem.*, 1983, **87**, 4548–4553.
- 99 H. Kunieda, K. Nakamura, H. Davis and D. F. Evans, *Langmuir*, 1991, **7**, 1915–1919.
- 100 W. Richtering, *Optical Methods and Physics of Colloidal Dispersions*, Springer, 1997, pp. 90–96.
- 101 R. Weigel, J. Läuger, W. Richtering and P. Lindner, *J. Phys. II*, 1996, **6**, 529–542.
- 102 J. E. Hunter and J. F. Fowler, *J. Surfactants Deterg.*, 1998, **1**, 235–239.
- 103 J. S. Pedersen and P. Schurtenberger, *Macromolecules*, 1996, **29**, 7602–7612.
- 104 W.-R. Chen, P. D. Butler and L. J. Magid, *Langmuir*, 2006, **22**, 6539–6548.
- 105 J. N. Israelachvili, D. J. Mitchell and B. W. Ninham, *J. Chem. Soc. Faraday Trans.*, 1976, **72**, 1525–1568.
- 106 J. N. Israelachvili, D. J. Mitchell and B. W. Ninham, *Biochim. Biophys. Acta*, 1977, **470**, 185–201.
- 107 Z. Sun, T. Feng and T. P. Russell, *Langmuir*, 2013, **29**, 13407–13413.
- 108 D. Chen, Z. Sun, T. P. Russell and L. Jin, *Langmuir*, 2017, **33**, 8961–8969.
- 109 G. Ciofani, V. Raffa, V. Pensabene, A. Menciasci and P. Dario, *Fullerenes Nano. Carbon Nanostruct.*, 2009, **17**, 11–25.
- 110 M. Granite, A. Radulescu and Y. Cohen, *Langmuir*, 2012, **28**, 11025–11031.
- 111 G. Beaucage, *J. Appl. Crystallogr.*, 1996, **29**, 134–146.
- 112 K. Mortensen and Y. Talmon, *Macromolecules*, 1995, **28**, 8829–8834.
- 113 M. Bohorquez, C. Koch, T. Trygstad and N. Pandit, *J. Colloid Interface Sci.*, 1999, **216**, 34–40.
- 114 G. Beaucage and D. Schaefer, *J. Non-Cryst. Solids*, 1994, **172**, 797–805.
- 115 G. Beaucage, *J. Appl. Crystallogr.*, 1995, **28**, 717–728.
- 116 A. Guinier, G. Fournet and C. Walker, *Small angle scattering of X-rays*, J. Wiley & Sons, New York, 1955.
- 117 P. Somasundaran and S. Krishnakumar, *Colloids Surf., A*, 1997, **123**, 491–513.



Graphene oxide (flat)